Stability-Constrained Aerodynamic Shape Optimization of Flying Wings

Charles A. Mader[*]

University of Toronto Institute for Aerospace Studies

Toronto, Ontario, Canada

Joaquim R.R.A. Martins[†]

Department of Aerospace Engineering, University of Michigan

Ann Arbor, Michigan

The optimal shape of flying wings for subsonic and transonic speeds is examined using a suite of tools developed around a three-dimensional, time-spectral Euler computational fluid dynamics solver. The first result in the study is a lift-constrained drag minimization, performed on an unswept, rectangular wing. When the spanwise twist distribution of the wing is varied the elliptic optimum predicted by low-speed inviscid theory can be reproduced. With this result as a reference, three different optimization formulations are explored. These consider the addition of bending moment constraints, static-stability constraints, and dynamic-stability constraints. In each case, the design space of the problem is explored using both planform and shape variables to determine the optimal shape. These techniques are used to show that the addition of stability constraints has a significant impact on the optimal surface shape of the wing. In particular, it is shown that at lower speeds, airfoil shape is sufficient to satisfy static-stability constraints, while dynamic-stability constraints require the addition of sweep. It is also shown that at higher speeds, airfoil shape is insufficient to satisfy either stability constraint, static or dynamic, and that the addition of sweep is necessary.

Nomenclature

$*^{t}$ Individual discipline feasible target variables

α Angle of attack

$\bar{c}$ Mean chord

---

[*]Research Associate, AIAA Member
[†]Associate Professor, AIAA Senior Member

$\bar{c}_{\text{ref}}$ Reference chord length

Δ_{FFD} Free form deformation volume control point movement, y direction

$\dot{q}$ Time derivative of q

λ Sweep

ω Short-period frequency

σ Bending stress

$\text{CG}_{\%}$ Center of gravity variable

θ_i Section twist

ζ Short-period damping ratio

A Wing area

A_1 Planform area

A_2 Calculated projected area

b Span

C_D Drag coefficient

C_L Lift coefficient

C_m Pitch moment coefficient

C_p Coefficient of pressure

C_{bend_x} x component of root bending moment

C_{bend_z} y component of root bending moment

C_{b} Total root bending moment coefficient

c_{root} Root chord

C_{f_x} Force coefficient in the x direction

C_{f_y} Force coefficient in the y direction

C_{f_z} Force coefficient in the z direction

C_{L_α} Derivative of C_L with respect to α

American Institute of Aeronautics and Astronautics

C_{m_x} Moment coefficient in the x direction

C_{m_y} Moment coefficient in the y direction

C_{m_z} Moment coefficient in the z direction

$C_{m_{\mathrm{CG}}}$ Pitch moment coefficient about the CG

$C_{m_{\mathrm{NP}}}$ Pitch moment coefficient about the NP

e Span efficiency factor

g Gravitational acceleration

h_{CG} Normalized streamwise position of the CG

h_{NP} Normalized streamwise position of the NP

I Second moment of area of beam/wing

I_y Pitch moment of inertia

K_n Static margin

L Generic length scale

M Bending moment

M_i Pitch moment derivative with respect to parameter i

n Vertical acceleration as a multiple of g

$P_{I_{zz}}$ Moment-of-inertia modifier

q Dynamic pressure

S_{ref} Reference area

t/c Thickness-to-chord ratio

u Forward aircraft velocity

V Velocity

w Vertical aircraft velocity

x_{bend} Bending reference point

x_{CG} Location of the CG

x_{ref} CFD moment reference location

y Height of beam/wing

Z_i Vertical force derivative with respect to parameter i

ATC   Analytical target cascading

BLISS   Bi-level integrated system synthesis

CAP   Control anticipation parameter

CFD   Computational fluid dynamics

CG   Center of gravity

CO   Collaborative optimization

CSSO   Concurrent subspace optimization

FFD   Free form deformation

IDF   Individual discipline feasible

M   Mach number

MAC   Mean aerodynamic chord

MDF   Multidisciplinary feasible

MDO   Multidisciplinary design optimization

NACA   National advisory committee for aeronautics

NP   Neutral point

OML   Outer mold line

SAND   Simultaneous analysis and design

XDSM   Extended design structure matrix

American Institute of Aeronautics and Astronautics

I.   Introduction

The design of flying-wing aircraft is a complex, coupled problem. In addition to the strong aerostructural coupling seen in typical aircraft design, there is a strong coupling between the aerodynamic efficiency of the outer mold line (OML) and the trim and stability of the aircraft. This strong coupling requires a delicate balance between optimizing the aircraft for aerodynamic performance and maintaining the necessary stability characteristics [1]. Thus, multidisciplinary design optimization (MDO) is an invaluable tool in flying-wing design. While stability characteristics have been considered in aircraft MDO using lower fidelity tools [2, 3, 4], as efficiency standards are increased, more accurate, higher fidelity analyses will be required in the design process to make the most of new configurations. Further, while high-fidelity aerodynamic optimization has matured significantly over the last twenty years [5, 6, 7, 8], and aerostructural optimization has made great strides over the last ten years [9, 10, 11], the ability to consider stability characteristics using high-fidelity aerodynamic information has not been incorporated. In this work, we examine a series of increasingly complex optimization problems to study the effects that various structural and stability constraints have on the optimal design. In particular, we examine the trade-offs between optimal aerodynamic performance and the limits imposed by structural and stability constraints. The consideration of stability is enabled by the recently developed time-spectral stability derivative method [12], which efficiently computes stability derivatives and their sensitivities using computational fluid dynamics (CFD).

The main body of this study is arranged in five sections. Section II provides a brief overview of the tools and methods used and gives references to other work with more details on each method or tool. Section III then provides a review of MDO methods with particular emphasis on the techniques used in this work. Section IV introduces the design problem and discusses the various optimization formulations that are used in the study. Finally, Section V presents the results, examining the qualitative and quantitative trends in the solutions.

II.   Methodology

The methodologies used to conduct this study are driven by two main factors: the desire to consider transonic aircraft, and the desire to consider stability constraints. The first consideration necessitates, at a minimum, the solution of the Euler equations using CFD. The second requires the computation of the stability characteristics of the aircraft along with their sensitivities with respect to the design variables of interest. In this work, we model the aerodynamics with the time-spectral Euler equations and use an adjoint method to generate the necessary gradients for the optimizations. The use of the time-spectral equations allows for the computation of the stability derivatives necessary for the various stability-constraint formulations used. Details on the time-spectral equations and the associated adjoint can be found in Mader and Martins [13].

In addition to the flow solver, which is the core component of this work, a number of other tools are necessary. These include tools for optimization, geometry handling, and mesh handling. We also need a variety of simple auxiliary analyses to compute the constraints. These components are described below.

A.   Optimization Algorithm

The optimization tool used in this work is `pyOpt` [14], a Python-based optimization framework that allows the user to access, through a common interface, a variety of numerical optimization packages. The cost of each CFD solution is relatively high and there are hundreds of design variables. To make this optimization problem tractable, we use a gradient-based optimizer in conjunction with an adjoint method for computing the gradients [13]. `pyOpt` provides interfaces to a variety of gradient-based optimizers, both open source and licensed. We have chosen to use the `pyOpt` interface to SNOPT [15], an SQP-based optimizer, because SNOPT is proficient at handling large nonlinear optimization problems.

B.   Geometry Modeling

The geometry model has a series of layers. The top layer is a conceptual design description based on simple planform variables. This level of the geometry is handled by `pyACDT` [16], a Python-based, object-oriented aircraft design tool. This tool models the planform of the aircraft and provides information for the conceptual-level mass and inertia computations used in the computation of the stability constraints.

The high-fidelity geometry representation is modeled by `pyPSG` [17]. This tool is used to create a watertight surface representation of the aircraft, a set of spline volumes enveloping the aircraft, and a set of reference axes inside the aircraft. The set of volumes enveloping the aircraft is used in conjunction with a free form deformation (FFD) technique [17] to handle the detailed geometry manipulations during the optimization. The surface points on the CFD mesh are embedded parametrically in these spline volumes, such that when the volumes are moved or deformed, the CFD surface mesh is modified as well. The reference axes are used to tie together the control points of the FFD volumes enveloping the aircraft. By tying the control points to a reference axis, we are able to create the effect of physical design variables such as sweep, twist, taper, area, span, and chord, which are more meaningful to a designer than the location of arbitrary control points. The geometry is structured such that the planform changes specified in the `pyACDT` geometry layer are transferred to the CFD surface mesh through these reference axes.

C.   Mesh Deformation

Once the CFD surface mesh has been deformed, that deformation needs to be propagated to the CFD volume mesh. This is handled using an efficient mesh deformation technique developed

American Institute of Aeronautics and Astronautics

by Kenway et al. [17]. The CFD mesh is represented by a coarse finite-element mesh, which is deformed using the perturbations of the coarse mesh surface nodes as input values. The finite-element equations are solved, and the large surface deformations are propagated to the remainder of the volume mesh. Then, an algebraic mesh deformation scheme, based on trans-finite interpolation, is used to propagate the surface deformations to the blocks immediately adjacent to the surface. This provides a fully updated volume mesh to the CFD solver.

D. Geometry Constraints

To make the results more realistic, we include two geometry constraints in the optimizations. The first is a set of thickness constraints, included to prevent the optimizer from making the wing unrealistically thin. These constraints are implemented by computing thicknesses at various locations in the wing and constraining those values to be no smaller than the initial values; the locations are defined by the user. We constrained the thickness to maintain the thickness of the NACA 0012 profile at the 1%, 50%, and 99% chords at ten evenly spaced stations along the wing.

The second geometry constraint is a constraint on the leading- and trailing-edge control points of the FFD volume. If these points are allowed to move freely, they can reproduce the same degrees of freedom as twist variables, producing an ill-posed optimization problem. To prevent this, we constrain the control points at each of the leading and trailing edges to move in equal and opposite directions so that the midpoint of the FFD does not move with the shape variable perturbations.

E. Center of Gravity Calculation

We implement a relatively simple wing center of gravity (CG) calculation. The method is derived from the work of Chai et al. [18], where the authors state that the wing CG for a normal transport wing is located between the fore and aft spars along the wing mean aerodynamic chord (MAC). Since flying wings are the focus of this study, we assume that this estimate of the wing CG is a reasonable estimate of the CG for the entire aircraft. Thus, we allow the CG to vary as a design variable over a range of one mean aerodynamic chord. As shown in Fig. 1, this range runs from the rear spar forward, where the rear spar is assumed to be at 75% of the MAC chord location.

F. Moment of Inertia Calculations

The calculations for the moments of inertia are based on first principles. We discretize the surface of the wing into a mesh of surface cells, each of which is assigned a thickness. The area, thickness, and density of each of these cells allows the wing to be represented as a mesh of lumped masses as shown in Fig. 2. We then use these masses to compute the moment of inertia of the wing skin. Because the first-principles method approximates only the moment of inertia of the wing skin, we add an additional multiplier to the computation to account for the remaining mass distribution
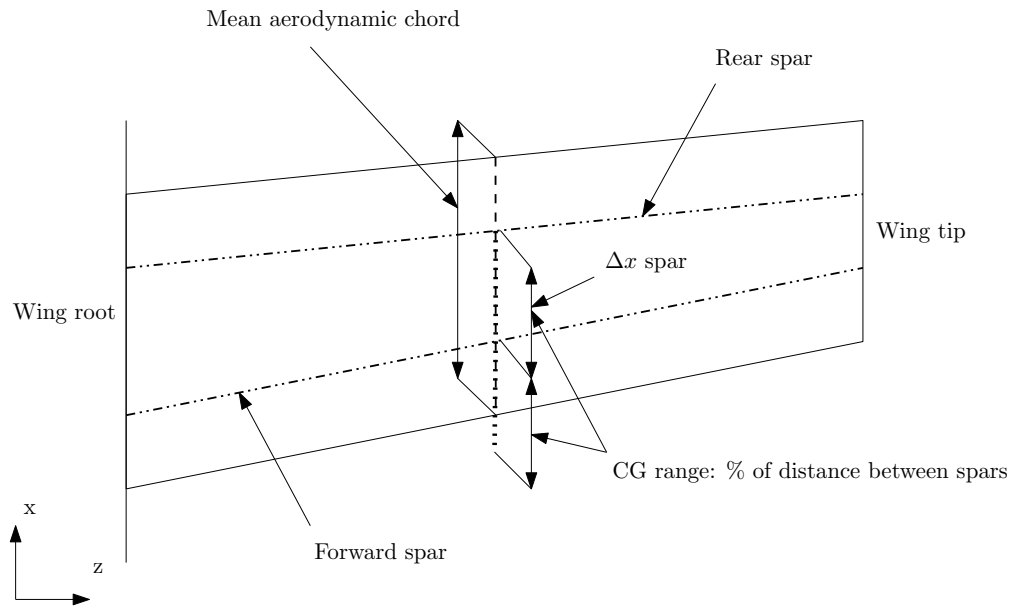
Figure 1. Diagram of CG calculation

in the aircraft. This parameter is given to the optimizer as a variable to allow it to satisfy the constraints in the dynamic-stability constrained optimization.

G.   Root Bending Moment Constraint

The root bending moment constraint is included to take into account the structural implications of the varying wing shapes. There are well known trade-offs between aerodynamic and structural performance for wings, the most prominent of which has to do with the effects of span. Increasing the span reduces the induced drag. However, for a given lift distribution and total lift, a span extension also increases the bending moment at the root of the wing. This in turn requires a heavier structure to support the aerodynamic load. A similar effect is caused by wing sweep. For shearing sweep—where individual sections of the wing are translated in the flow-wise direction to sweep the wing—the effective structural length of the wing increases as the wing is swept. This can be counteracted by reducing the span of the wing or washing out the wing tip to increase the portion of the lift generated on the inner portion of the wing. Both of these modifications introduce trade-offs between induced drag and wave drag at transonic Mach numbers. Therefore, if span and sweep are used as design variables, it is necessary to account for these trade-offs between aerodynamic performance and structural weight. We use the root bending moment as a proxy for the structural performance of the wing. The assumption implicit in this approach is that two wings with the same root bending moment require the same amount of material to support the load on the wing and thus have the same weight. This is a relatively simplistic assumption, but it serves as a useful metric for including structural considerations in the optimization.

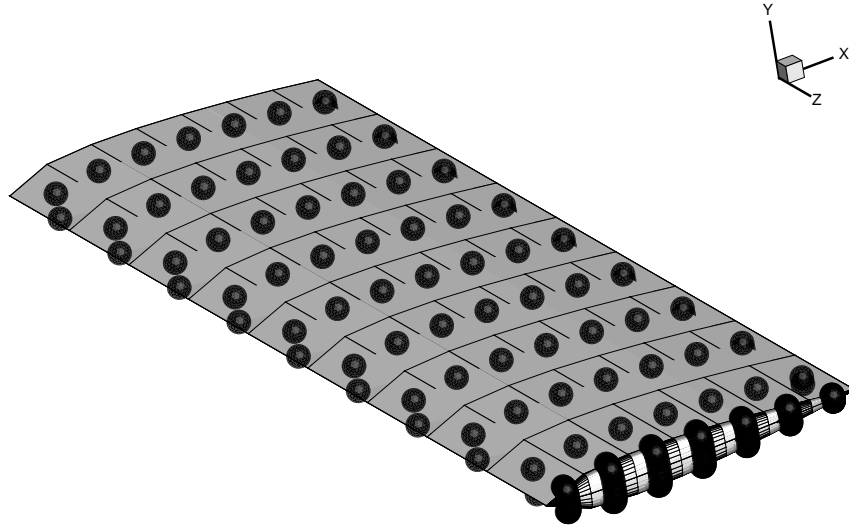   To compute the bending moment coefficient, we integrate the pressure over the aircraft to get

American Institute of Aeronautics and Astronautics

Figure 2. Discrete surface mesh with lumped masses at the cell centroids

the force and moment coefficients about a reference point, x_{ref}, which in this case is the CG, x_{CG}. This computation yields the values of C_{f_x}, C_{f_y}, C_{f_z}, C_{m_x}, C_{m_y}, and C_{m_z}, which are the force and moment coefficients in the three principal Cartesian axes. We then specify a bending reference point, x_{bend}, at the root of the wing. This is the point about which the net bending moment is calculated. We calculate the bending moment as follows:

$$
\begin{aligned}
C_{\mathrm{bend}_x} &= C_{m_x} + C_{f_y} \frac{x_{\mathrm{bend}_z} - x_{\mathrm{ref}_z}}{\bar{c}_{\mathrm{ref}}} - C_{f_z} \frac{x_{\mathrm{bend}_y} - x_{\mathrm{ref}_y}}{\bar{c}_{\mathrm{ref}}} \\
C_{\mathrm{bend}_z} &= C_{m_z} - C_{f_y} \frac{x_{\mathrm{bend}_x} - x_{\mathrm{ref}_x}}{\bar{c}_{\mathrm{ref}}} + C_{f_x} \frac{x_{\mathrm{bend}_y} - x_{\mathrm{ref}_y}}{\bar{c}_{\mathrm{ref}}} \\
C_{\mathrm{b}} &= \sqrt{C_{\mathrm{bend}_x}^2 + C_{\mathrm{bend}_z}^2}
\end{aligned}
\tag{1}
$$

where $\bar{c}_{\mathrm{ref}}$ is the reference chord length, C_{b} is the total root bending moment coefficient, and C_{bend_x} and C_{bend_z} are the Cartesian components of the root bending moment about the bending reference point at the wing root.

Figure 3 illustrates the various components of this calculation. Note that since the torsional component of the wing moment is nonzero, the effective bending moment is not necessarily aligned with the wing. Also note that as the wing is swept, this torsional component increases, causing the combined effective bending moment to sweep with the wing. Therefore, we assume that the wing can be supported normal to the effective total bending moment, regardless of the wing sweep and pressure distribution. Thus, only the total magnitude of the bending coefficient, C_{b}, is considered. Note that the reference value of C_{b} used to constrain the wing has a significant effect on the optimal
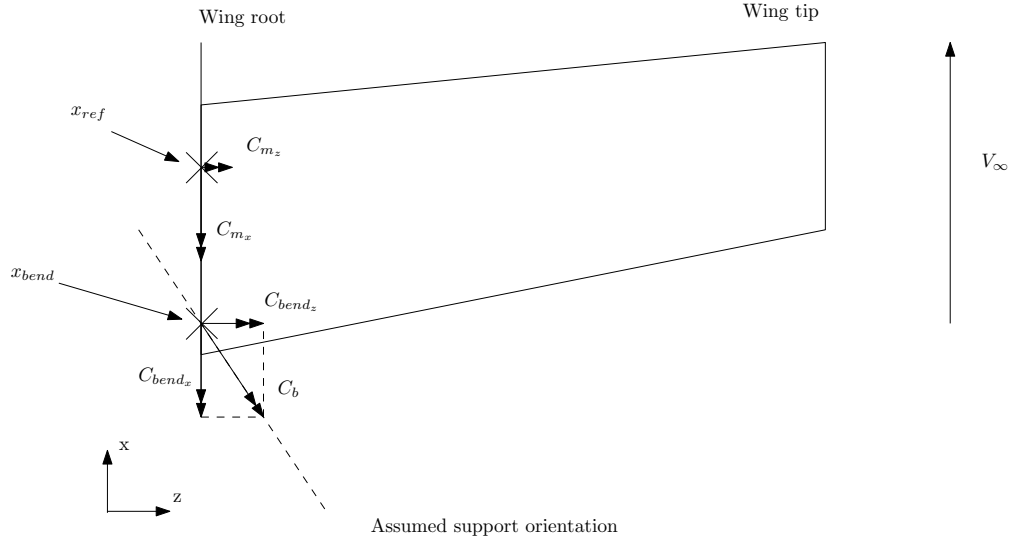
American Institute of Aeronautics and Astronautics

Figure 3. Bending moment calculation

design. We use the value from the elliptical optimum—computed at M = 0.5—as the reference value. We then scale this value with the root cross-section to ensure that as the optimizer increases the aspect ratio of the wing, the allowable bending moment is reduced to account for the reduced second moment of the area at the wing root. The reasoning behind this scaling is based on the definition of bending stress,

$$\sigma = \frac{My}{I}. \tag{2}$$

Rearranging to get an expression for the moment and performing a dimensional analysis yields

$$M \propto \frac{\sigma L^4}{L} = \sigma L^3. \tag{3}$$

Note that because we are assuming a constant t/c ratio, both the thickness and chord dimensions scale with L. Therefore, if we express the moment in terms of coefficients, with A constrained to be constant in the optimizations, we get:

$$C_{\text{bend}} \propto \frac{\sigma L^2}{qA}. \tag{4}$$

Thus, for constant qA, the allowable bending moment must be scaled with L^2 to enforce a constant allowable bending stress at the wing root. Note that in this specific case L is the ratio of the optimized root chord and the initial root chord of $1\,\text{m}$.

H. Stability Derivatives

The stability constraints used in this work are based on linear flight dynamic theory. This theory uses aircraft stability derivatives to represent aerodynamic characteristics of the aircraft in a

state-space model. We calculate the aircraft stability derivatives using the time-spectral stability derivative formulation developed by Mader and Martins [12]. This approach is similar to the methods presented by Murman [19] and Da Ronch et al. [20] and is motivated by the complex number $\dot{\alpha}$ derivative methodology outlined by Etkin [21]. It is essentially a forced oscillation technique. A time-spectral CFD solver is used to generate the solution for a prescribed oscillatory motion. This periodic solution is then used, with a linear regression technique, to generate estimates for the functionals of interest: the force or moment coefficient, the derivative of the coefficient with respect to the oscillating parameter, and the derivative of the coefficient with respect to the time derivative of the oscillating parameter. We are interested in the derivatives of the lift, drag, and pitch moment coefficients (C_L, C_D, C_m) with respect to α, q and their time derivatives, $\dot{\alpha}$, $\dot{q}$. The simple algebraic nature of this method allows it to be used in conjunction with an adjoint method to efficiently compute the necessary gradients.

I. Stability Constraints

One of the main contributions of this work is the development of a methodology that allows for the inclusion of CFD-based stability information in aerodynamic shape optimization. This section outlines how we use the stability derivatives and the resulting linear flight dynamics model to formulate stability constraints for the optimization problem. Two stability constraints are considered: one based on static stability and one based on dynamic stability. A discussion of other stability criteria for a flying-wing configuration can be found in Agenbag [22].

1. Static Longitudinal Stability

To develop a static-stability constraint, we turn to the definition of the static margin. First, consider the definition of the moment coefficient,

$$C_{m_{\mathrm{CG}}} = C_{m_{\mathrm{NP}}} + (h_{\mathrm{CG}} - h_{\mathrm{NP}})C_L, \tag{5}$$

where h_{CG} and h_{NP} are the streamwise locations of the CG and the neutral point respectively, normalized by the MAC. Differentiating with respect to α yields

$$\frac{\partial C_{m_{\mathrm{CG}}}}{\partial \alpha} = (h_{\mathrm{CG}} - h_{\mathrm{NP}})\frac{\partial C_L}{\partial \alpha} \tag{6}$$

or, using stability derivative notation,

$$C_{m_\alpha} = (h_{\mathrm{CG}} - h_{\mathrm{NP}})C_{L_\alpha}. \tag{7}$$

American Institute of Aeronautics and Astronautics

Defining the static margin, K_n, as the distance between the CG and the neutral point normalized by the MAC,

$$K_n = h_{\mathrm{NP}} - h_{\mathrm{CG}}, \tag{8}$$

and substituting this relationship back into Eq. (7) results in

$$C_{m_\alpha} = -K_n C_{L_\alpha}. \tag{9}$$

This can be rearranged as

$$K_n = -\frac{C_{m_\alpha}}{C_{L_\alpha}}. \tag{10}$$

Thus, by specifying a static margin, we can determine a meaningful value for C_{m_α}.

Up to this point, the discussion has been completely general and applicable to any aircraft. By examining Eqs. (5) and (7), we can gain insight into how the various stability conditions may be satisfied for the particular case of a flying wing. Equation (5) shows that the moment coefficient is dependent on the moment about the neutral point—which does not change with the angle of attack—and the location of the neutral point with respect to the CG. Thus, the optimizer can trim the aircraft by altering three parameters: the moment, the neutral point position, and the CG position. The moment coefficient about the neutral point is altered either by changing the airfoil shape—adding reflex to the airfoil—or by twisting down the wing tips on a swept wing. The neutral point of the aircraft is altered primarily by changing the sweep of the wing. Finally, the CG location of the aircraft can be altered by changing the sweep of the wing or by shifting the payload location. However, Eq. (7) shows that the neutral point and CG locations both impact C_{m_α} and hence the static margin. Thus, the optimizer must simultaneously adjust the wing sweep and shape as well as the payload location to trim the aircraft and create an acceptable static margin. These elements are discussed along with the results in Section V.

2. Short-Period Approximation

As a precursor to the discussion on the dynamic-stability constraint, we introduce the short-period approximation to the standard linear flight dynamic model. This approximation assumes that the variation in forward velocity (u) is negligible and that the short-period characteristics of the aircraft can be modeled by changes in the pitch rate (q) and the angle of attack (α) alone. In this case, the vertical velocity (w) is used in place of the angle of attack, where

$$\tan \alpha = \frac{w}{u}. \tag{11}$$

To begin, we define a simplified version of the flight dynamic model based on the degrees of

American Institute of Aeronautics and Astronautics

freedom described above, the details of which can be found in McRuer et al. [23]. This gives:

$$\begin{bmatrix} \Delta\dot{w} \\ \Delta\dot{q} \end{bmatrix} \begin{bmatrix} \frac{-Z_w}{m} & -u_0 \\ \frac{-M_{\dot{w}}Z_w}{I_y m} - \frac{M_w}{I_y} & \frac{-M_{\dot{w}}u_0}{I_y} - \frac{M_q}{I_y} \end{bmatrix} \begin{bmatrix} \Delta w \\ \Delta q \end{bmatrix} + \begin{bmatrix} Z_{\text{control}} \\ M_{\text{control}} \end{bmatrix} \begin{bmatrix} \Delta_{\text{control}} \end{bmatrix}. \tag{12}$$

Ultimately, as we show later in this section, the handling-quality analyses we are interested in require the frequency and damping ratio of the aircraft. These values can be determined from the characteristic equation of the 2×2 system in Eq. (12). As shown in McRuer et al. [23] the relevant characteristic equation is

$$s^2 + \left(\hat{M}_{\dot{w}}u_0 + \hat{M}_q + \hat{Z}_w \right) + \hat{Z}_w\hat{M}_q - \hat{M}_w u_o. \tag{13}$$

Comparing this to the typical second-order characteristic equation,

$$s^2 + 2\zeta\omega s + q^2, \tag{14}$$

yields

$$\omega = \sqrt{\hat{Z}_w\hat{M}_q - \hat{M}_w u_o} \tag{15}$$

and

$$2\zeta\omega = \left(\hat{M}_{\dot{w}}u_0 + \hat{M}_q + \hat{Z}_w \right) \tag{16}$$

or

$$\zeta = \frac{\hat{M}_{\dot{w}}u_0 + \hat{M}_q + \hat{Z}_w}{2\omega}. \tag{17}$$

We can now use the frequency and damping ratio of the short-period mode to evaluate the control anticipation parameter (CAP), which is used as the dynamic-stability constraint in this study.

3. Control Anticipation Parameter

The CAP technique quantifies the handling qualities of an aircraft based on its short-period characteristics. The fundamental idea behind this approach is that a pilot's ability to fly an aircraft precisely along a given flight path is related to their ability to anticipate the response of the aircraft. Bihrle [24] relates the pilot's ability to anticipate response to the ratio of the aircraft's instantaneous pitch acceleration and its steady-state normal acceleration:

$$\text{CAP} = \frac{\dot{q}}{\Delta n}. \tag{18}$$

However, these quantities are not necessarily simple to evaluate. Therefore, with a little rearranging, Bihrle [24] provides the following expression:

$$\text{CAP} = \frac{\omega_n^2}{n_\alpha} \tag{19}$$

where n_α is the change in lift force (in gravities) with angle of attack:

$$n_\alpha = \frac{\frac{1}{2}\rho V^2 S_{\text{ref}} C_{L_\alpha}}{g}. \tag{20}$$

We can now use the stability derivative methods and short-period approximation described earlier to compute the necessary values.

The United States Military has specified acceptable limits for the CAP and damping ratio for various combinations of aircraft and flight conditions [25]. For an aircraft at cruise (Category B), these limits are shown in Table 1.

Table 1. MIL-F-8785c handling-quality limits

	Damping Ratio Limits		CAP Limits	
	Lower Bound	Upper Bound	Lower Bound	Upper Bound
Level 1	0.30	2.0	0.085	3.6
Level 2	0.20	2.0	0.038	10.0
Level 3	0.15	-	0.038	-

III.   MDO Solution Architecture

An MDO architecture is the method used to handle the coupling between disciplines in a multidisciplinary optimization problem [26]. Over the years, numerous architectures have been developed to handle this coupling including monolithic architectures such as MDF [27], IDF [27], and SAND [28] and decompositional architectures such as CO [29], CSSO [30], BLISS [31], and ATC [32].

In this work we use a hybrid of the MDF and IDF approaches. The analyses used herein can be decomposed into four disciplines: geometry, aerodynamics, structures, and flight dynamics. The task of coupling the disciplines is simplified greatly by the fact that, for the analyses used in this work, there is no feedback between disciplines. Thus, the tightly coupled MDF architecture amounts to a sequenced evaluation of the disciplines. However, when adjoint methods are used, coupling the derivatives of the various disciplines is not straightforward. This motivates the use of the IDF architecture, which requires only the individual discipline sensitivity analyses and greatly simplifies the computation of accurate gradients.

American Institute of Aeronautics and Astronautics

Despite this apparent advantage, there are some disciplines for which tight coupling is a better choice. The coupling between the geometry and the aerodynamics, for example, requires a large number of coupling variables: there are typically thousands of mesh points on the surface. In an IDF architecture, this would add thousands of variables and constraints to the problem, which would unnecessarily increase the complexity of the optimization. By tightly coupling the geometry surface to the aerodynamics, we can remove these coupling variables.

The other area where tight coupling makes sense is between the aerodynamics and the structures. The bending coefficient calculation is based on six force and moment coefficients, of which only one, C_{m_z}, is already present in the optimization. Separating these two disciplines would require the solution of five additional adjoint problems per optimization iteration. By tightly coupling the aerodynamics and structures, we can reduce this to a single additional adjoint problem for the bending coefficient. A detailed overview of each optimization problem is presented in the following section. Note that all of the optimization diagrams that follow are presented in the extended design structure matrix (XDSM) format of Lambe and Martins [33].

IV.   Optimization Study Definition

The baseline wing used for the current study is a straight, rectangular wing with a NACA 0012 airfoil profile. The wing has a half span of three meters and a chord of one meter, giving the wing an aspect ratio of six. The wing has a taper ratio of one and a leading-edge sweep angle of zero degrees. The details of the geometry are summarized in Table 2. This test case is based on the induced-drag validation case proposed by Hicken and Zingg [8], who demonstrate that one can use this wing, with sections twisted about the trailing edge, to reproduce the elliptical distribution outlined by lifting-line theory. In particular, they highlight the use of a straight trailing edge, with spanwise sections twisted about the edge, to minimize the impact of nonplanar effects in the wake. We use this configuration as the initial geometry in this set of optimizations. The twist-only optimization outlined in Section C reproduces the elliptical result and can be used as a point of comparison for the remaining optimizations. This provides a means of quantifying the effect of the various stability constraints on the optimal solution. All of the optimization results are computed on a 1,105,920-cell mesh. The mesh has a C-O topology and is split into 32 blocks, with the surface mesh having 97 points spanwise and 81 points from the leading edge to the trailing edge on each of the top and bottom surfaces of the wing. The farfield boundary is approximately 15 chords from the wing and the off-wall spacing of the mesh is 1×10^{-3} m at the leading edge and 5×10^{-4} m at the trailing edge with a hyperbolic spacing in between.

A.   Mesh Convergence

To demonstrate the accuracy of the mesh used, we have performed a mesh convergence study, the results of which are shown in Table 3. As the table shows, the mesh is sufficiently refined, with

American Institute of Aeronautics and Astronautics

Parameter	Value
Half wing area (m)	3.0
Half wing span (m)	3.0
Chord (m)	1.0
Leading edge sweep (deg.)	0.0
Taper ratio	1.0
Wing tip washout (deg.)	0.0
Wing dihedral	0.0

Table 2. Baseline wing: Geometry specifications

errors of less than 1% for C_L, C_D, and C_{L_α} and an error of 1.1% for C_{m_α}.

Case	C_L	C_D	C_{L_α}	C_{m_α}
138,000 cell	0.262161	0.004065	5.00924	1.19912
1,100,000 cell	0.261608	0.003787	4.99286	1.18342
8,800,000 cell	0.261322	0.003769	4.98115	1.17374
Exact (Richardson extrapolation)	0.261228	0.003763	4.97724	1.17051
1,100,000 cell % error	0.146	0.621	0.314	1.10

Table 3. Grid refinement results

B. Design Variables

Two sets of design variables are used: one involving only planform variables and one involving planform variables as well as 280 surface-shape design variables. These surface-shape design variables—the control points of the FFD volume—modify the surface shape of the wing and affect both its streamwise and spanwise profile. Table 4 shows the primary design variables that alter the shape and planform of the wing as well as the variables that affect the flow condition of the test case, while Table 5 shows the compatibility design variables introduced as a result of the hybrid IDF-MDF architecture used.

Design variable	Symbol	Lower bound	Upper bound
Angle of attack (deg.)	α	-15	15
Section twist at 9 sections (deg.)	θ_i	-10	10
Area (m)	A_1	2.9	3.2
Span (m)	b	2.0	3.2
Sweep (deg.)	λ	0	42.5
Center of gravity variable	$CG_\%$	-1	1
I_{zz} Modifier	$P_{I_{zz}}$	0.5	10,20,30
FFD control points: y-offset (m)	Δ_{FFD}	-0.05	0.05

Table 4. Primary design variables and their bounds

Note that not all design variables are used for all cases. A number of the variables listed are present as a function of the IDF architecture mentioned previously and are therefore present only

Design variable	Symbol	Lower bound	Upper bound
Moment reference location (m)	x_{CG}^t	−20	20
Rotation point (m)	x_{CG}^t	−20	20
Chord (m)	c_{root}^t	0.5	1.4
Target MAC (m)	MAC^t	−5	5
Target drag coefficient	C_D^t	−2	2
Target lift curve slope	$C_{L_\alpha}^t$	0	20
Target moment curve slope	$C_{m_\alpha}^t$	−20	0
Target $\dot\alpha$ derivative	$C_{m_{\dot\alpha}}^t$	−20	20
Target pitch derivative	$C_{m_q}^t$	−20	0

Table 5. Compatibility design variables and their bounds

when the associated disciplines are included in the problem statement.

C. Reference Problems

1. Baseline Problem

As a first step, we formulate a problem to find the angle of attack, α, and CG location, x_{CG}, that yield a trimmed aircraft at the target value of C_L for each Mach number. This problem is formulated as:

$$
\begin{aligned}
\text{minimize} \quad & C_D \\
\text{w.r.t.} \quad & \alpha, x_{\mathrm{CG}} \\
\text{subject to} \quad & C_{L_{\mathrm{ref}}} - C_L \leq 0 \\
& C_m = 0
\end{aligned}
\tag{21}
$$

Note that the lift-coefficient constraint is formulated as an inequality constraint rather than an equality constraint. Because the induced drag is proportional to C_L^2, reducing C_L also reduces the drag. Therefore, the optimizer will drive C_L as close to zero as possible, making an upper limit on C_L, i.e., an equality constraint, unnecessary.

2. Twist Optimization

As a second benchmark, we perform a twist-only optimization for the subsonic case (Mach = 0.5). This problem is designed to reproduce the elliptical result from lifting-line theory and is formulated

American Institute of Aeronautics and Astronautics

as:

$$\begin{aligned}
&\text{minimize} && C_D \\
&\text{w.r.t.} && \alpha, \theta_i, \mathbf{CG}_\%, x_{\mathrm{CG}}^t && (22) \\
&\text{subject to} && C_{L_{\mathrm{ref}}} - C_L \leq 0 \\
&&& C_m = 0 \\
&&& x_{\mathrm{CG}}^t - x_{\mathrm{CG}} = 0
\end{aligned}$$

In this optimization, twist variables θ_i are added to control the lift distribution, and the full CG calculation is added to control the location of the CG. Note that the aircraft is trimmed during the optimization by forcing the pitch moment coefficient about the CG, C_m, to be zero. However, since the location of the CG is allowed to move—through the variable $\mathrm{CG}_\%$—the aircraft can be trimmed without changing the aerodynamic shape.

3. Bending Moment Constrained Optimizations

As a third and final benchmark, we consider an aerodynamic optimization problem with a structural constraint. In this problem, span (b), sweep (λ), and area (A_1) are added as additional design variables and a root bending moment constraint, C_b, is added to keep these variables within sensible bounds. The value of the bending coefficient at the root is that of the elliptical optimal solution at Mach $= 0.5$. Additional compatibility constraints for the root chord, c_{root}, and the calculated area, A_2, are also added to account for the new flexibility. This problem is formulated as:

$$\begin{aligned}
&\text{minimize} && C_D \\
&\text{w.r.t.} && \alpha, \theta_i, A_1, b, \lambda, \mathbf{CG}_\%, \Delta_{\mathrm{FFD}}, c_{\mathrm{root}}^t, x_{\mathrm{CG}}^t, \mathbf{MAC}^t && (23) \\
&\text{subject to} && C_{L_{\mathrm{ref}}} - C_L \leq 0 \\
&&& C_m = 0 \\
&&& C_b - C_{b_{\mathrm{ref}}} = 0 \\
&&& A_2 - A_{\mathrm{ref}} = 0 \\
&&& x_{\mathrm{CG}} - x_{\mathrm{CG}}^t = 0 \\
&&& \mathbf{MAC} - \mathbf{MAC}^t = 0 \\
&&& c_{\mathrm{root}} - c_{\mathrm{root}}^t = 0
\end{aligned}$$

Figure 4 graphically depicts the data and process flow for the bending constrained problem. Note that the twist optimization and the baseline problem are subsets of this optimization and can be visualized by removing the necessary variables from Fig. 4.
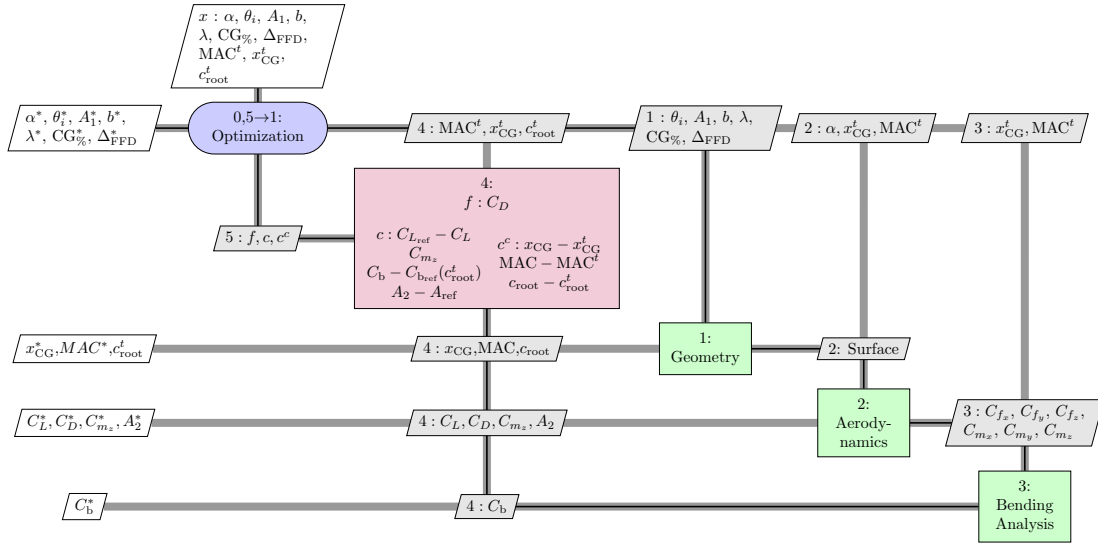
American Institute of Aeronautics and Astronautics

Figure 4. XDSM for the root bending moment constrained problem

D. Static-Stability Constrained Problems

The first stability constrained formulation is based on the static margin. By introducing this constraint we can ensure that the optimal design has the desired static margin. This formulation is as follows:

$$
\begin{aligned}
\text{minimize} \quad & C_D \\
\text{w.r.t.} \quad & \alpha, \theta_i, A_1, b, \lambda, \text{CG}_\%, \Delta_{\text{FFD}} \\
& c_{\text{root}}^t, x_{\text{CG}}^t, \text{MAC}^t, C_{L_\alpha}^t, C_{m_\alpha}^t \\
\text{subject to} \quad & C_{L_{\text{ref}}} - C_L \leq 0 \\
& C_m = 0 \\
& K_{n_{\text{ref}}} - K_n \leq 0 \\
& C_{\text{b}} - C_{\text{b}_{\text{ref}}} = 0 \\
& A_2 - A_{\text{ref}} = 0 \\
& x_{\text{CG}} - x_{\text{CG}}^t = 0 \\
& \text{MAC} - \text{MAC}^t = 0 \\
& c_{\text{root}} - c_{\text{root}}^t = 0 \\
& C_{L_\alpha} - C_{L_\alpha}^t = 0 \\
& C_{m_\alpha} - C_{m_\alpha}^t = 0
\end{aligned}
\tag{24}
$$

Note that K_n is the static margin and that additional constraints have been added for $C_{L_\alpha}^t$ and $C_{m_\alpha}^t$ corresponding to the additional IDF target variables that have been added for the computation of

American Institute of Aeronautics and Astronautics

the static-margin constraint.

E. Dynamic-Stability Constrained Problems

The dynamic-stability formulation used in this work is based on the CAP parameter described in Section II. This formulation builds on the previously described static-margin formulation and can be written as:

$$
\begin{aligned}
\text{minimize} \quad & C_D \\
\text{w.r.t.} \quad x = \quad & \alpha, \theta_i, A_1, b, \lambda, \text{CG}_\%, \Delta_{\text{FFD}}, c_{\text{root}}^t, x_{\text{CG}}^t, \text{MAC}^t, \\
& C_D^t, C_{L_\alpha}^t, C_{m_\alpha}^t, C_{m_{\dot{\alpha}}}^t, C_{m_q}^t \\
\text{subject to} \quad & C_{L_{\text{ref}}} - C_L \leq 0 \\
& C_m = 0 \\
& K_{n_{\text{ref}}} - K_n \leq 0 \\
& 0.085 \leq CAP \leq 3.6 \\
& 0.3 \leq \zeta_{sp} \leq 2.0 \\
& A_2 - A_{\text{ref}} = 0 \\
& x_{\text{CG}} - x_{\text{CG}}^t = 0 \\
& \text{MAC} - \text{MAC}^t = 0 \\
& c_{\text{root}} - c_{\text{root}}^t = 0 \\
& C_D - C_D^t = 0 \\
& C_{L_\alpha} - C_{L_\alpha}^t = 0 \\
& C_{m_\alpha} - C_{m_\alpha}^t = 0 \\
& C_{m_{\dot{\alpha}}} - C_{m_{\dot{\alpha}}}^t = 0 \\
& C_{m_q} - C_{m_q}^t = 0
\end{aligned}
\tag{25}
$$

We have added two primary constraints to the static-margin optimization, a CAP constraint and a ζ_{sp} constraint. These constraints define the appropriate limits for the dynamic-stability parameters. The range of allowable CAP values constrains the allowable short-period frequency, and the damping ratio, ζ_{sp}, is constrained directly. We have also added IDF constraints for C_D^t, $C_{m_{\dot{\alpha}}}^t$, and $C_{m_q}^t$ to reflect the addition of these variables for the computation of the dynamic-stability parameters. Figure 5 depicts the solution process for this formulation. The static-margin case is a subset of this case and can be visualized by removing the dynamic-stability constraints and their associated variables from the figure.

American Institute of Aeronautics and Astronautics
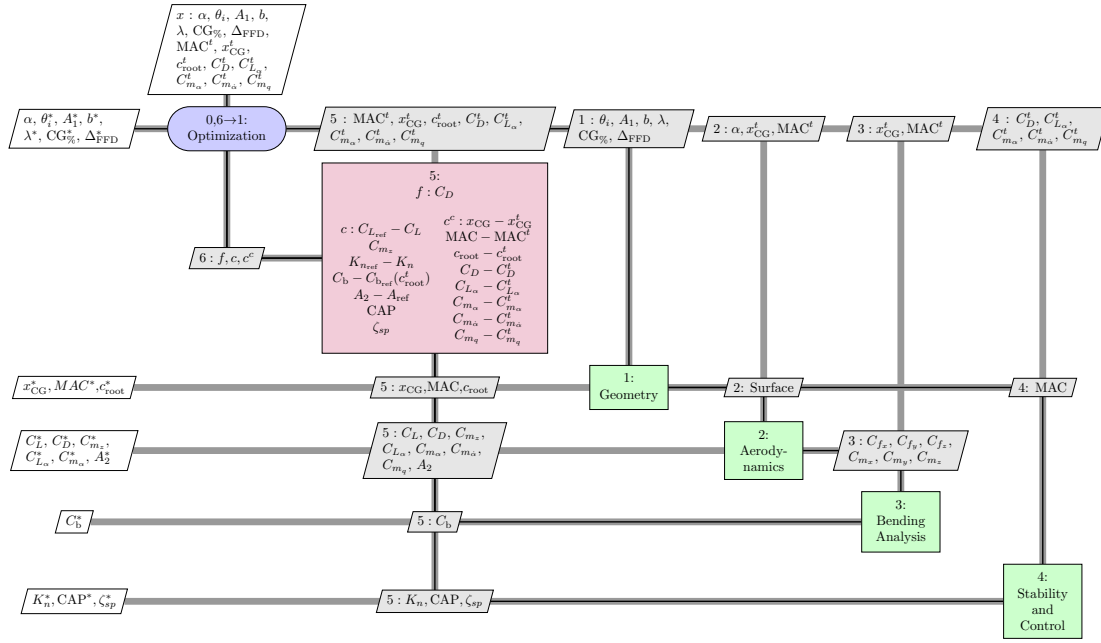
Figure 5. XDSM for the CAP constrained problem

V. Results

This section summarizes our results and findings. We present the results of the various formulations in order, identifying the effect of each constraint on the optimal solution. The optimizations are conducted at M = 0.5, 0.7, and 0.85 respectively to compare the effects of the subsonic and transonic flow regimes on the solution. A short summary of the most significant parameters is shown in Tables 6 through 10. The table results are sorted by Mach number and design variable set and will be referred to throughout the following discussion. All optimizations have been converged to $C_L = 0.30000$ and $C_m = 0.000001$.

A. Reference Problems

1. Baseline cases

The solutions for M = 0.5, 0.7, and 0.85 are shown in Figs. 6 through 8. The solutions at the three different Mach numbers each have different characteristics. The solution at $M = 0.5$ is fully subsonic, with a correspondingly peaky C_p distribution on the airfoil. Both the neutral point of the wing and the required center of gravity to trim are slightly forward of the wing quarter chord. This generates a C_{m_α} of 0.002 with a corresponding static margin of -0.04%, so the baseline wing is mildly unstable at M = 0.5. The drag coefficient for this case is 49.5 counts. The $M = 0.7$ case is just starting into the transonic regime and the inner half of the wing exhibits a weak shockwave near the leading edge. The location of the center of gravity to trim the aircraft is slightly further forward than in the M = 0.5 case but is still near the quarter chord. The neutral point is also shifted slightly

forward. This generates a C_{m_α} of 0.087 with a corresponding static margin of -1.49%. Thus, the M = 0.7 baseline case is slightly more unstable than the fully subsonic case. As expected, the drag coefficient increases in this case, to 55.7 counts. The M = 0.85 case is fully in the transonic regime and exhibits a strong shockwave on the aft half of the airfoil. As a result, the neutral point and the center of gravity location to trim are significantly farther back, near the half chord. Because both the CG and the neutral point are shifted, the instability is actually smaller than for the M = 0.7 case, giving a C_{m_α} of 0.055 and a static margin of -0.73%. However, the drag for this case is the highest of the three at 399 counts. Note that the free stream parameters (pressure and density) have been scaled such that the dynamic pressure q is the same for all cases.
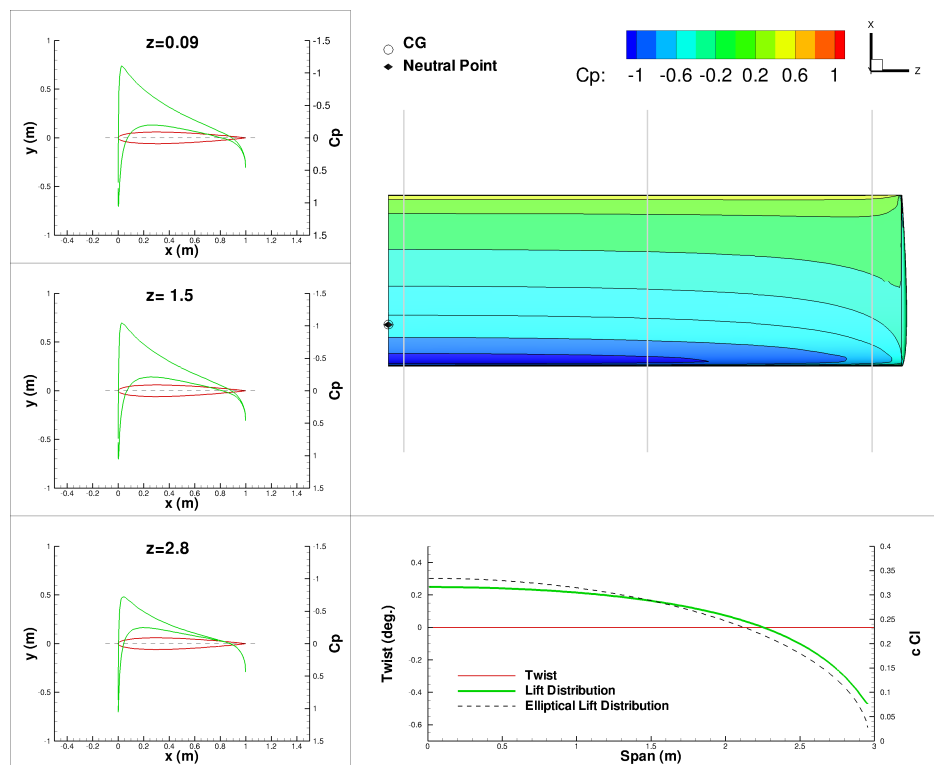
Figure 6. Baseline problem: M = 0.5, $e = 0.964$

2.   *Twist-Only Case*

The twist-only formulation yields the solution shown in Fig. 9. The optimal lift distribution achieved with this formulation closely approximates that of the elliptical solution. The exception to this is the area near the tip; this is because this location consists of complex three-dimensional flows that violate the assumptions used to derive the elliptical result. Further, the predicted drag of the twist optimized wing is 48.9 counts, within 2.5% of the theoretical value of 47.7 counts for this wing. This leads to a span efficiency of 0.977.

American Institute of Aeronautics and Astronautics
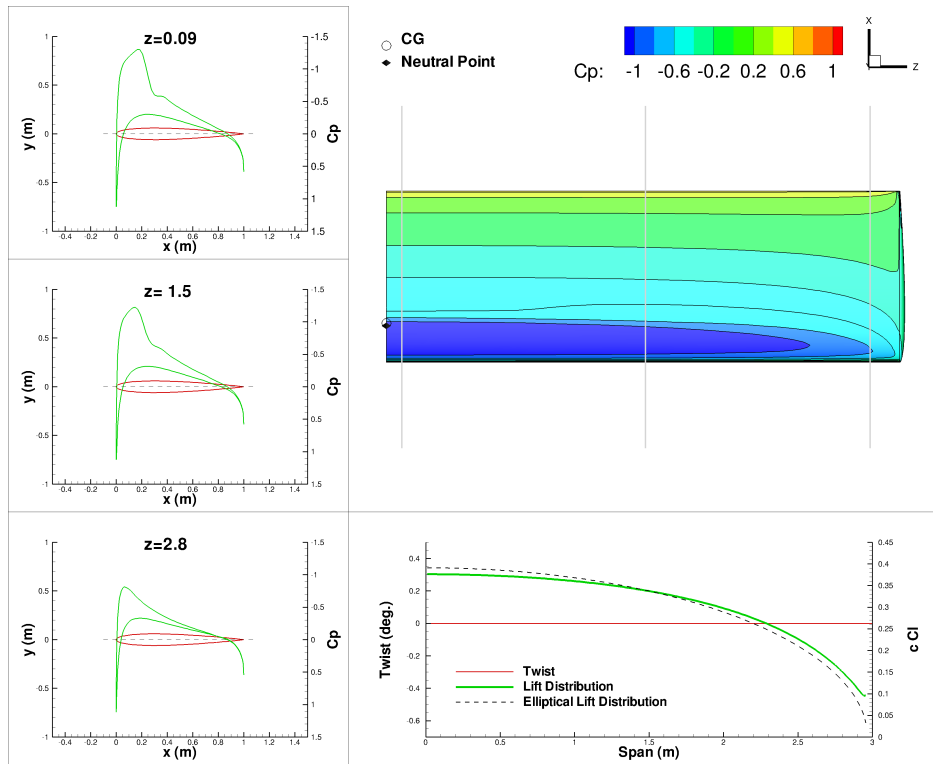
Figure 7. Baseline problem: M = 0.7
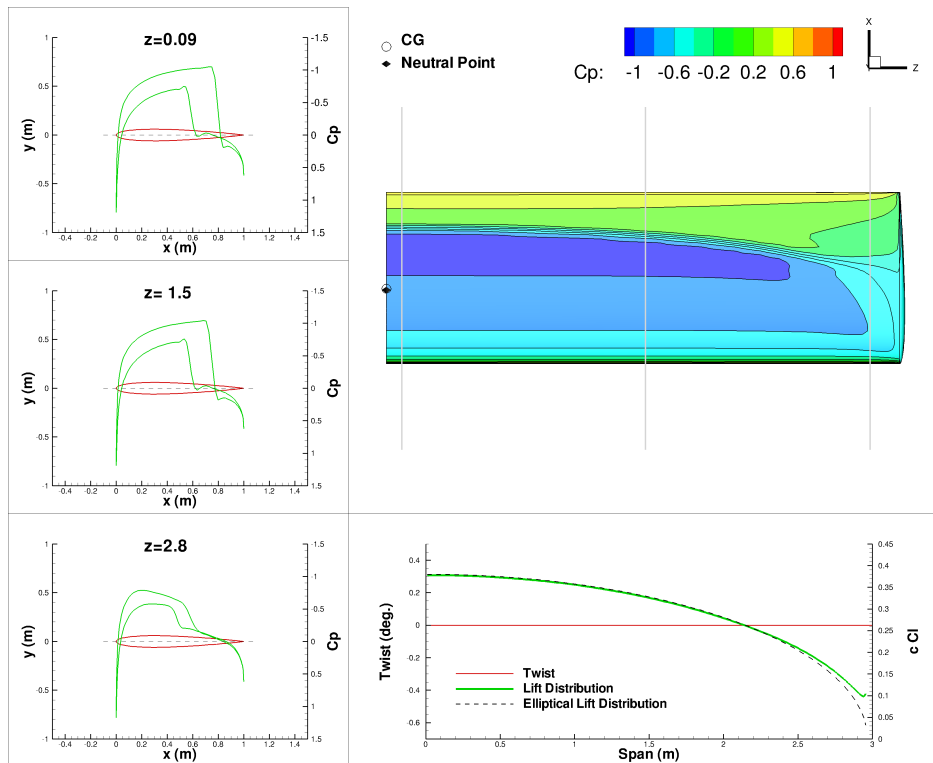
Figure 8. Baseline problem: M = 0.85

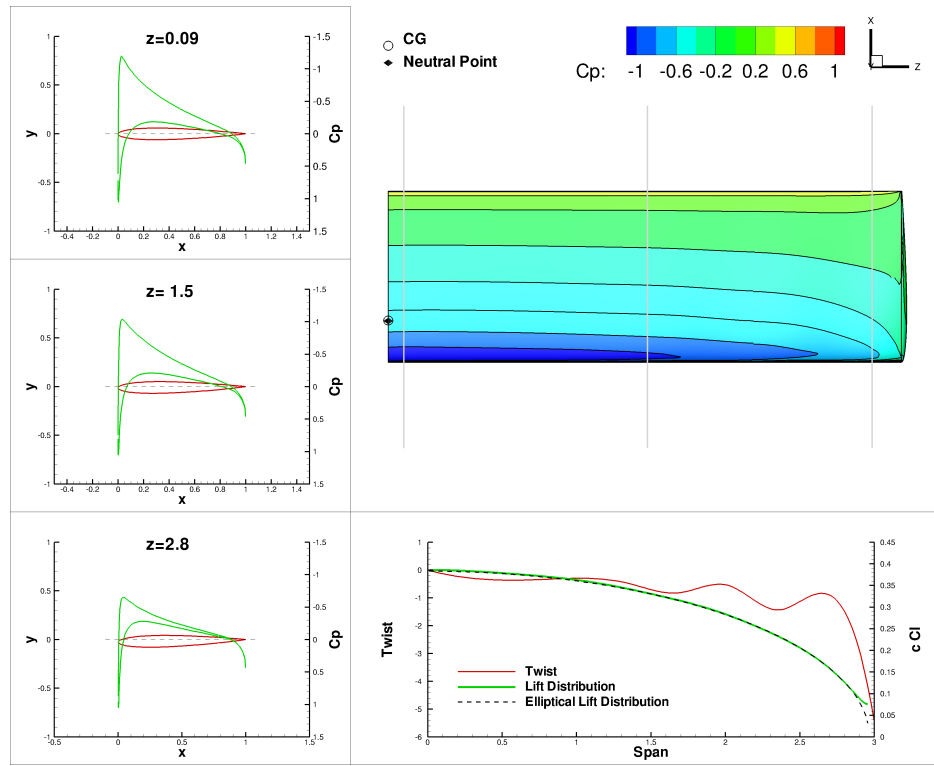American Institute of Aeronautics and Astronautics

Figure 9. Twist optimization: M = 0.5, $e = 0.977$

3. Bending Moment Constrained Cases

The root bending moment constrained optimizations have the same design variable flexibility as the stability constrained cases described in Sections B and C. Therefore, they should be able to produce shapes with lower drag than those for cases with stability constraints. These optimizations provide the best indication of how much performance is sacrificed to ensure that the stability constraints are satisfied. The results for the planform-only optimizations are shown in Figs. 10 and 11, and the results including shape variables are shown in Figs. 12 and 13. Note that there is no shape optimization result for the $M = 0.5$ case, because the airfoil shape has little impact on the drag of a subsonic wing in inviscid flow.

Comparing the elliptical solution shown in Fig. 9 to the bending constrained case at $M = 0.5$, shown in Fig. 10, we observe some subtle yet important differences. In the bending constrained case, the optimizer takes advantage of the span variable to reduce the induced drag. The added flexibility of the span variable allows the optimizer to reduce the drag an additional 1.4% from the twist-only optimum, from 48.9 to 48.2 counts. The extended span can be seen in Fig. 10, which compares the optimized wing to the original wing, shown as a black outline. Note that this increase in span is limited by the allowable root bending moment and comes with a corresponding movement away from an elliptical lift distribution.

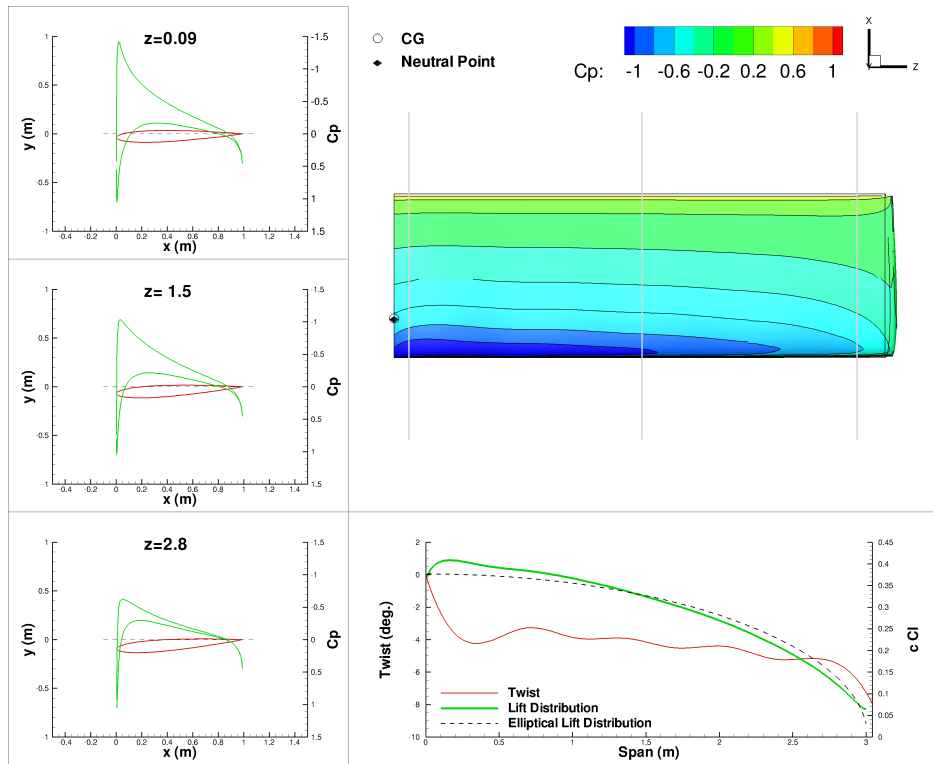In the $M = 0.7$ case, shown in Fig. 11, the optimizer adds a significant amount of sweep to

Figure 10. Bending moment constrained optimization: Planform variables only, M = 0.5, $e = 0.964$
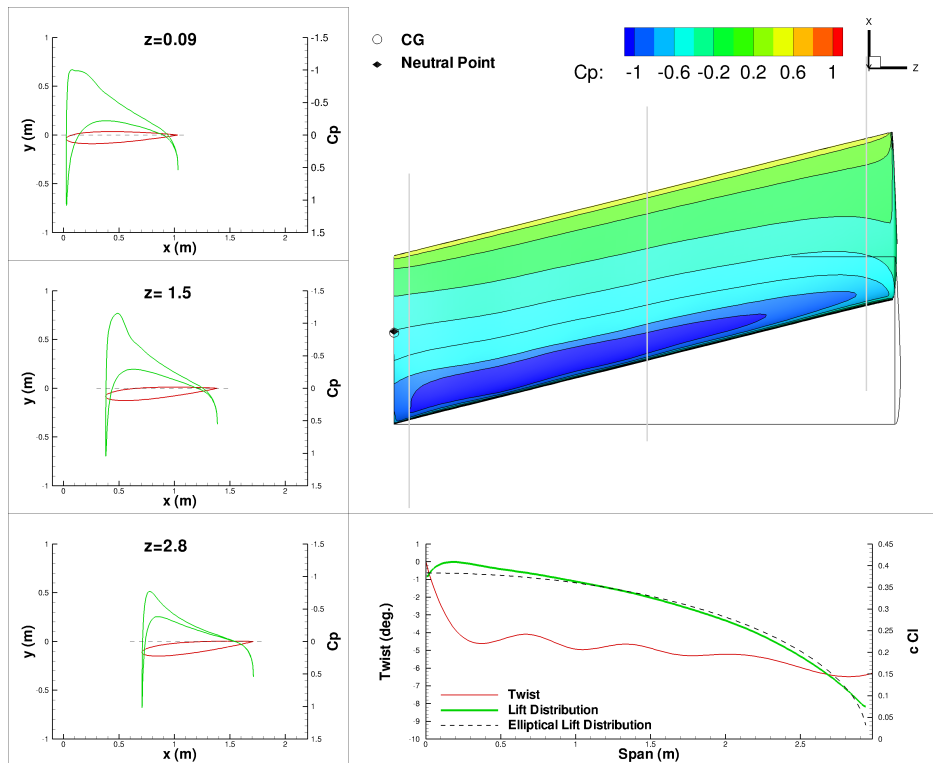

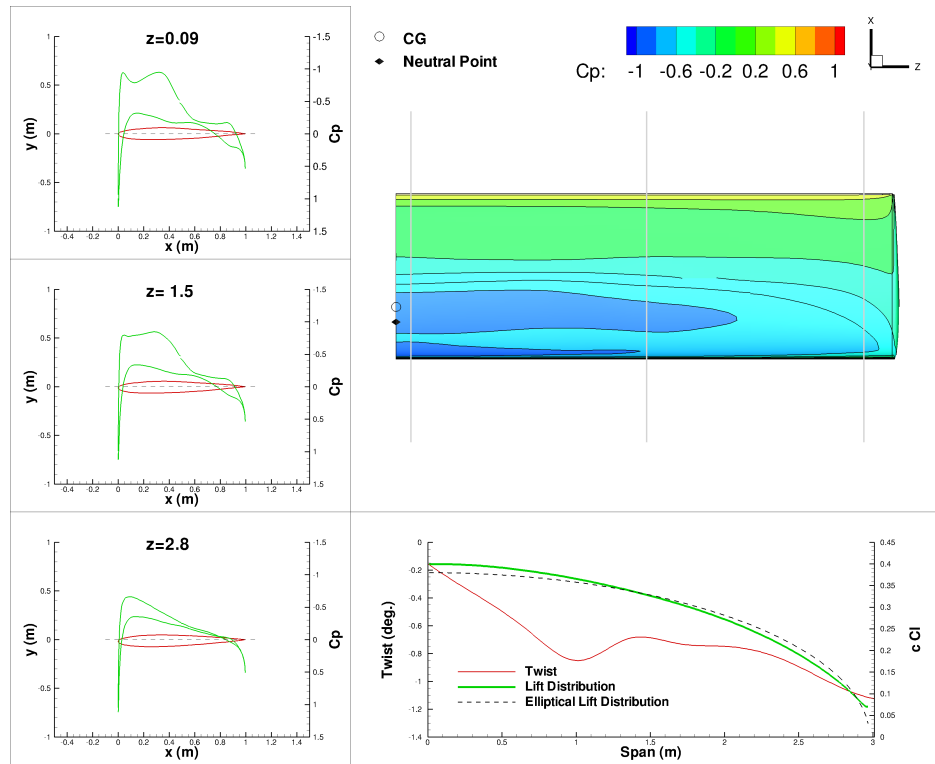**Figure 11. Bending moment constrained optimization: Planform variables only, M = 0.7**

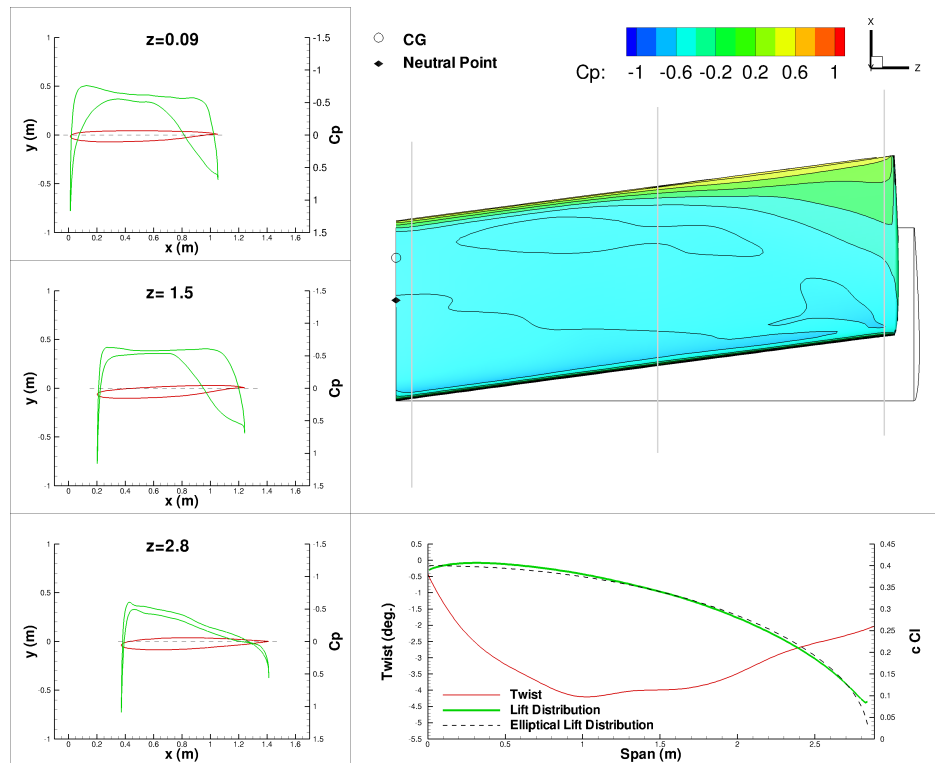**Figure 12. Bending moment constrained optimization: Planform and shape variables, M = 0.7**

Figure 13. Bending moment constrained optimization: Planform and shape variables, M = 0.85

the wing. This causes a trade-off between induced drag and wave drag. The added sweep reduces the effective Mach number normal to the wing leading edge, thereby reducing the strength of the leading-edge shock. With sufficient sweep, the Mach number normal to the leading edge of the wing is reduced below the critical Mach number, eliminating the shock wave and the corresponding wave drag. However, adding sweep increases the effective root bending moment. Thus, as sweep is added, the span must be reduced to meet the bending constraint. This is evident in the difference in span between the M $= 0.5$ case shown in Fig. 10 and the M $= 0.7$ case shown in Fig. 11. The net result is that the planform-only M = 0.7 case has a drag coefficient of 52.1 counts, lower than the baseline M = 0.7 case at 55.7 counts but higher than the M = 0.5 bending constrained case at 48.2 counts. Note that because of the addition of sweep and twist, this case now has a positive static margin of 0.75%.

When shape variables are added, the need for sweep to reduce wave drag is eliminated and, as shown in Fig. 12, the optimizer does not sweep the wing, allowing for a larger span. Further, there is now a significant change in the C_p distribution on the wing. The individual sections now show a rooftop pressure profile at the leading edge, allowing the maximum section C_p to stay below the critical C_p for the wing, thereby eliminating the wave drag on the wing. As a result, the drag is significantly reduced, to 49.7 counts, within 1.5 counts of the subsonic result. Note that the planform is now similar to the optimal M $= 0.5$ planform in Fig. 10. However, it is also important to note that without any stability constraint, the optimizer has produced a result that has a negative static margin of the order of 10%.

At M $= 0.85$, the optimizer produces the features typical of supercritical transonic airfoils for the individual airfoil sections. The sections show a rooftop C_p profile and are highly aft-loaded. However, even with these transonic airfoils, the wave drag is not entirely eliminated, so the optimizer introduces some sweep in the design to mitigate this effect. This added sweep causes a corresponding reduction in the span to maintain the required bending moment. This produces a wing with a drag coefficient of 57.9 counts, significantly better than the 399 counts of the initial wing but not as good as the 49.7 counts of the M = 0.7 wing. Note that because of the aft-loaded nature of these airfoils, the neutral point of the wing is significantly forward of the required CG location for trimmed flight, leading to a highly unstable wing with a static margin of -23.5%.

B.   Static-Stability Constrained Problems

The planform-only, static-margin constrained optimization at M $= 0.5$, shown in Fig. 14, shows an increase in sweep relative to the baseline case. The optimizer adds sweep and wash-out to trim the aircraft for a more forward CG position. In this case, the magnitude of the changes is sufficient to generate the necessary separation between the neutral point and the CG for a 5% static margin. Note that because of the static-margin constraint, the drag coefficient has now increased to 51.2 counts, an increase of 6% relative to the bending constrained case. When shape variables
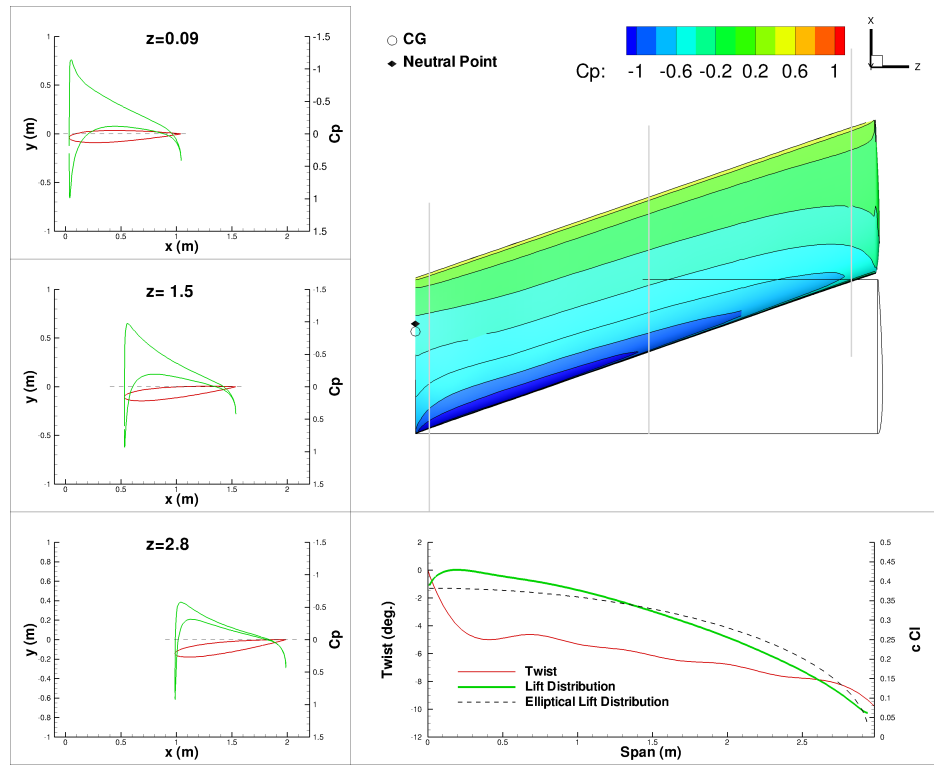
Figure 14. K_n **constrained optimization: Planform variables only, M = 0.5,** $e = 0.944$

are added, this additional sweep is not necessary to stabilize the aircraft. As shown in Fig. 15, the optimizer is able to use the shape variables to modify the C_p to achieve the same effect. In this case, the C_p distribution, especially near midspan, has developed negative lift near the trailing edge, which alters the $C_{m_{\text{NP}}}$ of the wing. This allows the optimizer to shift the CG forward—stabilizing the wing—using $\text{CG}_\%$ while still maintaining a trimmed state. Because the wing is in a stable trimmed state without sweep, there is no increase in the bending moment associated with sweep. Therefore, the optimizer is again able to increase the span from the baseline value of three meters. This produces a drag coefficient of 48.0 counts, essentially equivalent to that of the bending constrained case.

In the planform-only optimization at M $= 0.7$, the optimizer again adds sweep and twist to create separation between the neutral point of the wing and the CG location of the aircraft while maintaining a trimmed state. As can be seen in Fig. 16 there is now visible separation between the neutral point and the CG location. Once again, the sweep added to satisfy the static margin requires a span reduction and the resulting drag coefficient is 53.2 counts, higher than that for the bending constrained case. Again, the addition of shape variables allows the optimizer to unsweep the wing without sacrificing performance. As shown in Fig. 17, the optimizer uses the shape variables to alter the C_p distribution of the wing to trim the wing in a stable state. In this case, in addition to adding the negative lift near the trailing edge, the optimizer has flattened the C_p distribution at the leading edge of the wing, eliminating the pressure peak and thereby reducing the wave drag. Thus,
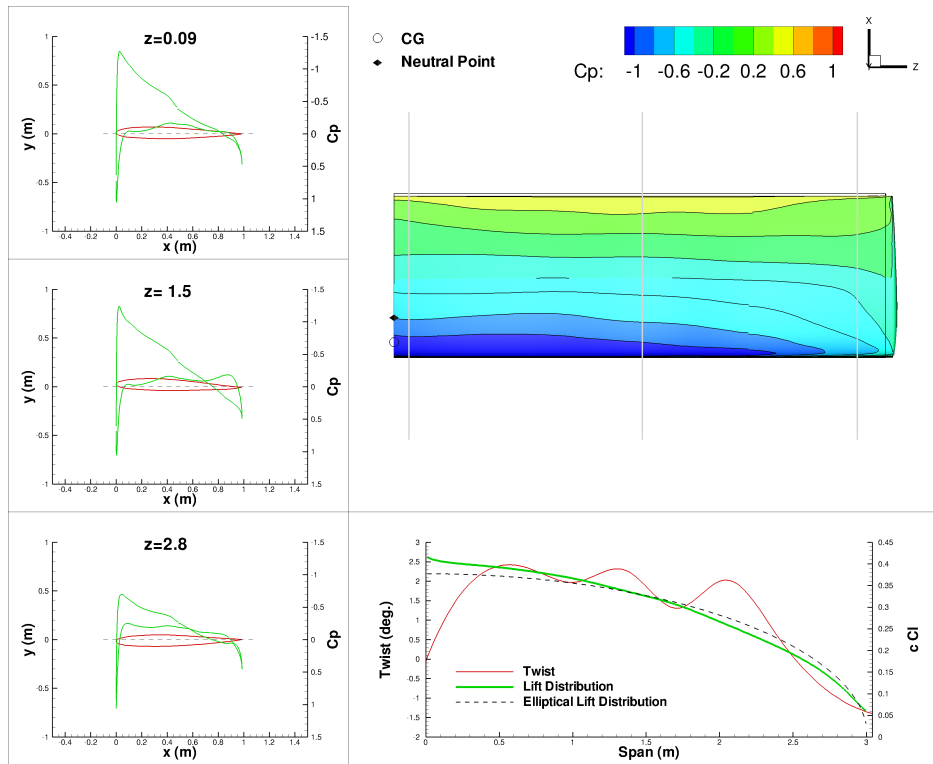
American Institute of Aeronautics and Astronautics

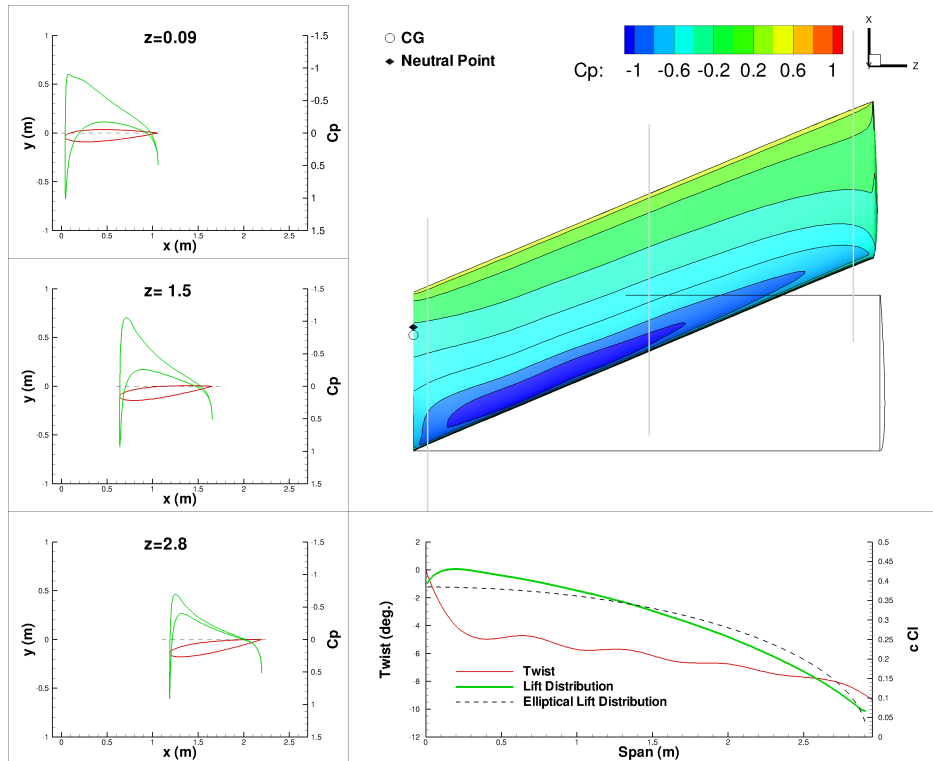**Figure 15.** K_n **constrained optimization: Planform and shape variables, M = 0.5,** $e = 0.968$

Figure 16. K_n **constrained optimization: Planform variables only, M = 0.7**

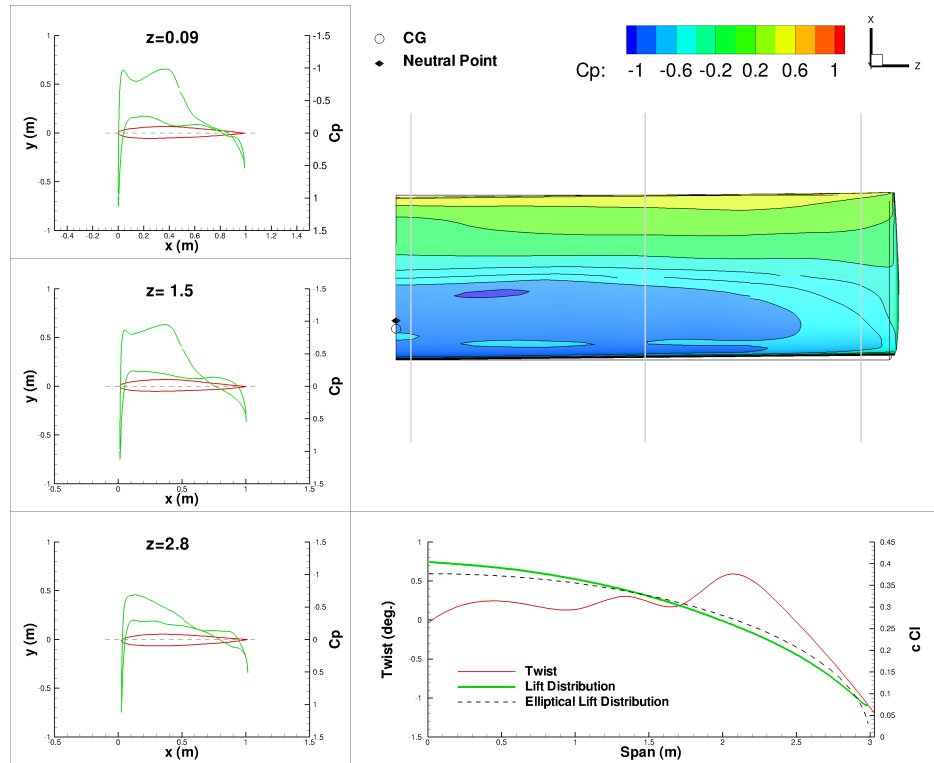the total drag for the case is 49.4 counts, in line with that for the bending constrained case.

Figure 17. K_n **constrained optimization: Planform and shape variables, M = 0.7**

The M $= 0.85$ case, shown in Fig. 18, is physically a more challenging problem for the optimizer. As in the previous bending constrained case, the optimizer attempts to reduce the wave drag with the airfoil shape. However, it is unable to produce the heavily aft-loaded airfoils that are optimal for this case because they lead to an unstable design. As a result, it is forced to compromise between reducing the drag and satisfying the static-margin constraint. These compromises show up in different ways at different sections of the wing. At the wing root, the C_p profile is spread over the entire chord of the section with significant lift generated at both the leading and trailing edges and relatively little lift mid-chord. The mid-wing section exhibits a rooftop C_p distribution over the front half of the foil, helping to reduce the wave drag of the wing. However, the addition of the static-margin constraint prevents the optimizer from extending this trend over the entire foil. As a result, there is a fairly constant amount of lift generated over the forward two-thirds of the foil with negative lift at the trailing edge. The optimizer has also added more sweep to the wing than in the comparable bending constrained case. As discussed earlier, this reduces the effective Mach number that the wing sees and allows tip washout to contribute to the wing trim.

In addition to this general discussion, there are two specific secondary characteristics that are worth highlighting. First, the optimizer adds a significant loading to the bottom surface of the leading edge of the wing at the root. This forward loading helps to reduce the moment of the root section. Also, the optimizer has developed an interesting inflection in the camber of the mid-wing

American Institute of Aeronautics and Astronautics

airfoil. At the trailing edge, the airfoil starts to develop the high camber shape typical of transonic airfoils, but partway to the trailing edge the foil develops reflex to help reduce the moment of the wing.
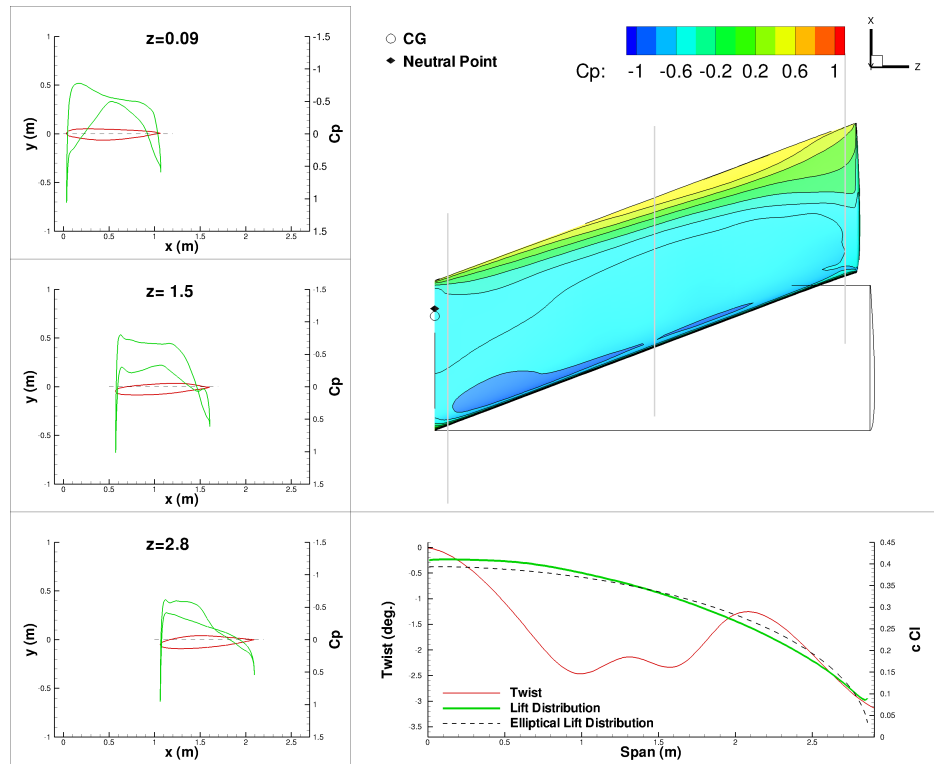

Figure 18. K_n **constrained optimization: Planform and shape variables, M = 0.85**

An interesting feature of this result is that it has produced a solution with only 56.4 counts of drag, lower than the 57.9 counts for the bending constrained case. The latter solution turns out to be a local optimum. By restarting the bending constrained problem at the static-margin constrained optimum, we get the optimal solution listed as bending V2 in Table 10, which is essentially the same as the static-margin constrained optimal solution. Thus, the static-margin constraint prevents the optimization from falling into the local optimum produced in the initial bending constrained case, producing the lower drag result.

C. Dynamic-Stability Constrained Problems

The CAP constrained optimizations add dynamic-stability constraints to the problem. This requires the consideration of extra stability derivatives and the mass moment of inertia of the aircraft. The optimal solution for the CAP constrained planform-only optimization at M = 0.5 (Fig. 19) is essentially the same as the static-margin result from Fig. 14: it has 51.3 counts, within 0.1 counts of the static-margin solution. This is because the moment-of-inertia multiplier is able to raise the moment of inertia sufficiently to satisfy the CAP and damping constraints. If the moment-of-inertia multiplier were limited to a smaller value, the optimal solution would likely be more highly swept
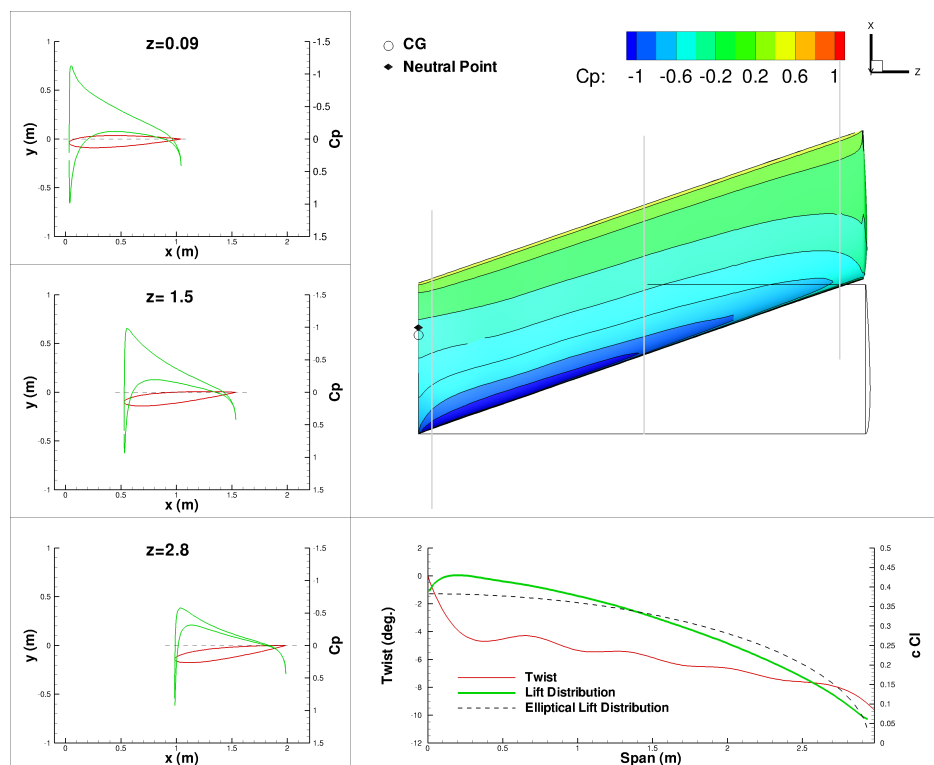
with a larger static margin and a higher drag.

Figure 19. CAP constrained optimization: Planform variables only, M = 0.5, $e = 0.942$

An interesting result from the addition of the dynamic constraints is that the addition of the shape variables no longer produces an unswept wing. As shown in Fig. 20, the optimal solution now has almost 20 degrees of sweep. This results largely from the need to maintain a sufficiently high moment of inertia to satisfy the damping requirements. As a result, the optimal solution still has 51.5 counts of drag, essentially the same as for the cases without shape variables. Another interesting side effect is that the section profiles no longer exhibit any reflex at the trailing edge. This is because the optimizer is now able to use sweep and tip washout to trim the aircraft without any additional penalty, so the C_p distribution is not required to add reflex to do so.

As for the previous CAP constrained cases, at M $= 0.7$ the shape variables are not sufficient to allow the optimizer to reduce the sweep of the wing to zero. Again the optimal results from the bending constrained case and the static-stability constrained cases have insufficient damping to satisfy the dynamic constraints, so even with shape variables, additional sweep is required to satisfy the frequency and damping constraints. As a result, the CAP constrained case produces a drag of 50.9 counts, more than a full count higher than that of the bending and static-margin constrained cases. Note that the added sweep causes the static-margin constraint to be inactive, although the mid-span section still develops a significant amount of reflex.

At M $= 0.85$, the CAP constrained result is essentially the same as the static-margin constrained result, differing by only 0.2 drag counts. Because the shape variables are not sufficient
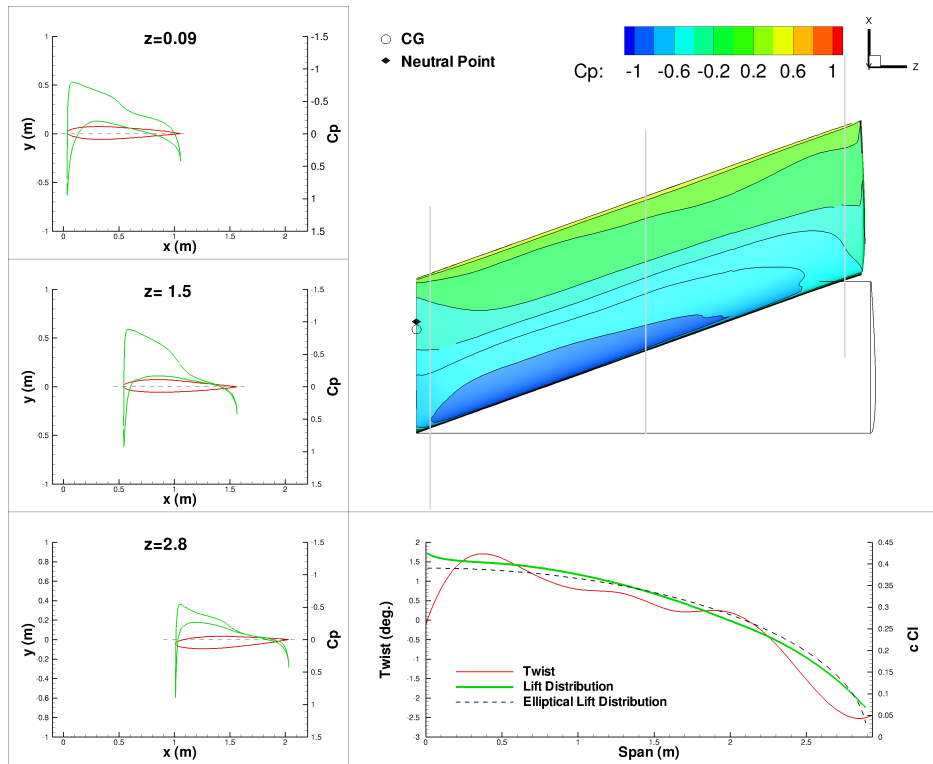
American Institute of Aeronautics and Astronautics

Figure 20. CAP constrained optimization: Planform and shape variables, M = 0.5, $e = 0.970$
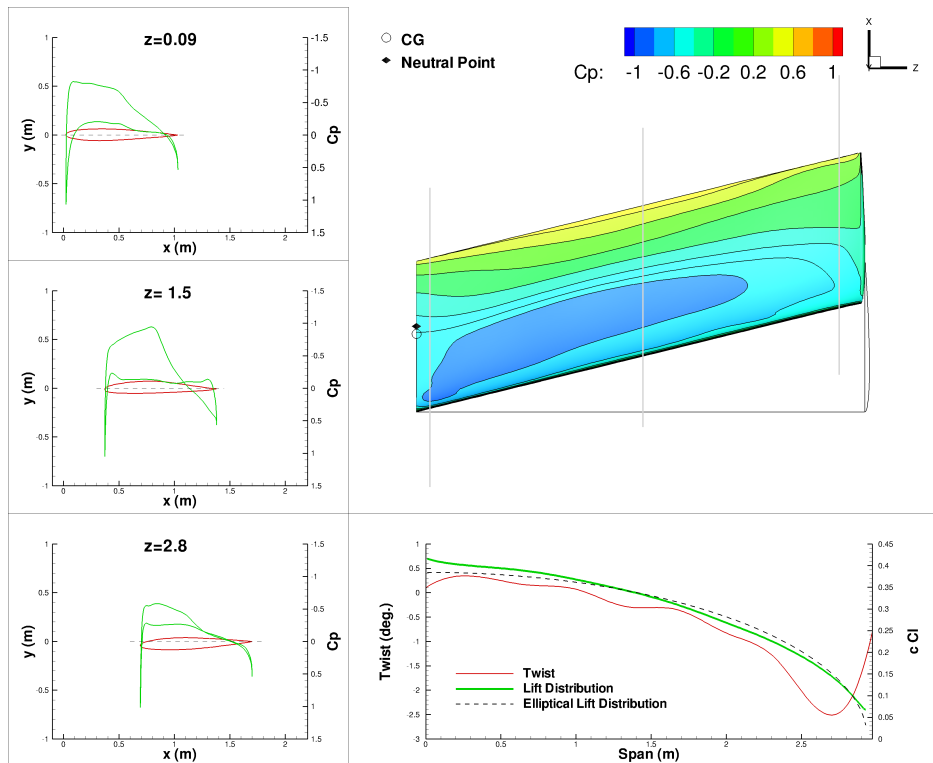
Figure 21. CAP constrained optimization: Planform and shape variables, M = 0.7

American Institute of Aeronautics and Astronautics

to allow the sweep to be completely eliminated at the higher Mach number, the static-margin case has enough sweep to ensure dynamic stability given a sufficient moment of inertia. Thus, the optimal result exhibits the same combinations of C_p distributions and planform variables as in the static-margin constrained case.
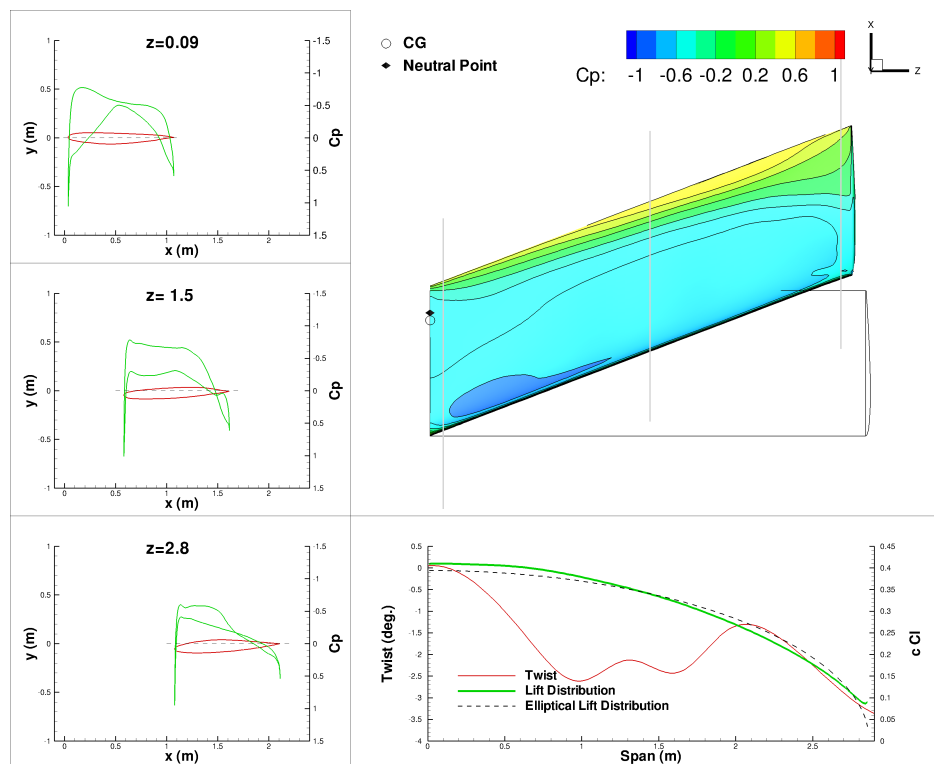

Figure 22. CAP constrained optimization: Planform and shape variables, M = 0.85

D. Convergence Histories

The convergence histories for the M $= 0.7$ cases are shown in Fig. 23. This figure shows the wide range of convergence rates for the various optimization problems. Surprisingly, the bending constrained case with shape variables takes the fewest iterations. One would expect the simplest optimization, the bending constrained case with planform-only variables, to converge most rapidly. However, this turns out not to be the case. On the other hand, as expected, the static-margin and CAP constrained cases with shape variables take the longest. This seems to indicate a relatively flat design space around the optimal solution. Note that these cases were converged to a tolerance of 5×10^{-5}, while the remainder of the cases were converged to a tolerance of 1×10^{-6}. Also note that the CAP constrained optimization with shape variables was started from the static-margin constrained optimum, so it has been shown starting at iteration 77, the end of the static-margin constrained optimization.

Parameter	Baseline	Elliptic	Bending	K_n	CAP
C_D	0.004954	0.004888	0.004817	0.005123	0.005133
C_{m_α}	0.002242	0.013867	0.029788	-0.246456	-0.246417
K_n (%)	-0.044805	-0.277744	-0.595908	4.999788	5.000118
e (%)	0.963761	0.976806	0.963537	0.943660	0.941934
CAP	0.000258	-0.015125	-0.037377	0.167942	0.168177
ζ_{sp}	8.047202	-0.000000	-0.000000	0.301925	0.301636
ω_n (rad/s)	0.065557	-0.000000	-0.000000	1.651115	1.652217
I_{zz} (kg m^2)	244.664280	242.153023	228.835160	494.760972	493.932604
α (deg.)	3.434484	4.042761	7.545133	9.065110	8.899279
λ (deg.)	0.000000	0.000000	0.000000	19.280100	19.250614
b (m)	3.000000	3.000000	3.042917	2.981338	2.981104
$P_{I_{zz}}$	10.000000	10.000000	10.000000	10.000000	10.000000

Table 6. NACA 0012 wing: Planform-only optimization results, 1107 k cells, M = 0.5

Parameter	K_n	CAP
C_D	0.004801	0.005149
C_{m_α}	-0.752988	-0.246065
K_n (%)	15.092049	5.000230
e (%)	0.968178	0.970392
CAP	0.586254	0.164005
ζ_{sp}	0.161038	0.299986
ω_n (rad/s)	3.142237	1.621730
I_{zz} (kg m^2)	403.325544	517.368619
α (deg.)	3.057671	3.051991
λ (deg.)	0.000000	19.888040
b (m)	3.040392	2.932521
$P_{I_{zz}}$	10.000000	10.000000

Table 7. NACA 0012 wing: Shape optimization results, 1107 k cells, M = 0.5

VI.   Conclusions

In this work, we explored the effects of static- and dynamic-stability constraints on the optimal shape of flying wings. The results showed that stability constraints have a significant impact on the optimal shape of the wing. In the subsonic regime and the lower end of the transonic regime, airfoil shape can be used to satisfy the static-stability constraints without significant degradation in performance. For these flow regimes, using airfoil shape is preferable to using wing sweep and twist to satisfy the static-stability requirements. At higher transonic Mach numbers, the degradation in performance is unavoidable, and the addition of sweep is necessary, regardless of the airfoil shape, to achieve satisfactory results. The same can not be said for the dynamic-stability constrained cases. The study showed that for the subsonic and low transonic cases, sweep was required, regardless of the airfoil shape, to raise the damping ratio of the aircraft to acceptable levels. At the higher speed in the transonic regime, the static-stability constrained results required sufficient sweep to be feasible for both the static- and dynamic-stability constraints. Thus, the results of this study

American Institute of Aeronautics and Astronautics

Parameter	Baseline	Bending	K_n	CAP
C_D	0.005570	0.005207	0.005325	0.005325
C_{m_α}	0.087088	-0.043966	-0.284135	-0.284114
K_n (%)	-1.491942	0.745596	4.999817	4.999817
CAP	-0.055895	0.020482	0.087320	0.087312
ζ_{sp}	-0.000000	0.672371	0.310233	0.310233
ω_n (rad/s)	-0.000000	0.631212	1.272602	1.272483
I_{zz} (kg m^2)	417.494607	623.660078	963.347405	963.470201
α (deg.)	2.933511	7.613268	8.590863	8.557310
λ (deg.)	0.000000	14.106302	22.861602	22.864088
b (m)	3.000000	2.980515	2.953919	2.953687
$P_{I_{zz}}$	16.184566	16.184566	16.184566	16.184566

Table 8. NACA 0012 wing: Planform-only optimization results, 1107 k cells, M = 0.7

Parameter	Bending	K_n	CAP
C_D	0.004973	0.004939	0.005090
C_{m_α}	0.539667	-0.298319	-0.302163
K_n (%)	-9.112122	4.999844	5.121750
CAP	-0.378485	0.129099	0.099087
ζ_{sp}	-0.000000	0.277583	0.299995
ω_n (rad/s)	-0.000000	1.609959	1.389344
I_{zz} (kg m^2)	380.807451	611.432529	847.763119
α (deg.)	2.987315	3.008049	3.282016
λ (deg.)	0.000000	0.529970	13.921081
b (m)	3.010364	3.029077	2.972135
$P_{I_{zz}}$	20.000000	20.000000	20.000000

Table 9. NACA 0012 wing: Shape optimization results, 1107 k cells, M = 0.7

underline the importance of considering both static- and dynamic-stability considerations in the design of flying-wing aircraft.

Acknowledgements

Parameter	Baseline	Bending	Bending V2	K_n	CAP
C_D	0.039898	0.005792	0.005654	0.005640	0.005619
C_{m_α}	0.055392	2.566048	-0.498659	-0.484800	-0.489347
K_n (%)	-0.729501	-23.522592	5.303884	4.999816	5.051372
CAP	-0.036492	-0.975527	0.065181	0.086524	0.086135
ζ_{sp}	-0.000000	-0.000000	0.361718	0.308502	0.309052
ω_n (rad/s)	-0.000000	-0.000000	1.429235	1.644602	1.639253
I_{zz} (kg m^2)	316.346371	416.989558	1356.125815	993.139864	1010.020857
α (deg.)	2.169667	3.437140	3.643754	3.643078	3.665365
λ (deg.)	0.000000	7.609797	20.970647	20.849705	21.144092
b (m)	3.000000	2.881879	2.899737	2.901532	2.898588
$P_{I_{zz}}$	21.988981	21.988981	21.988981	21.988981	21.988981

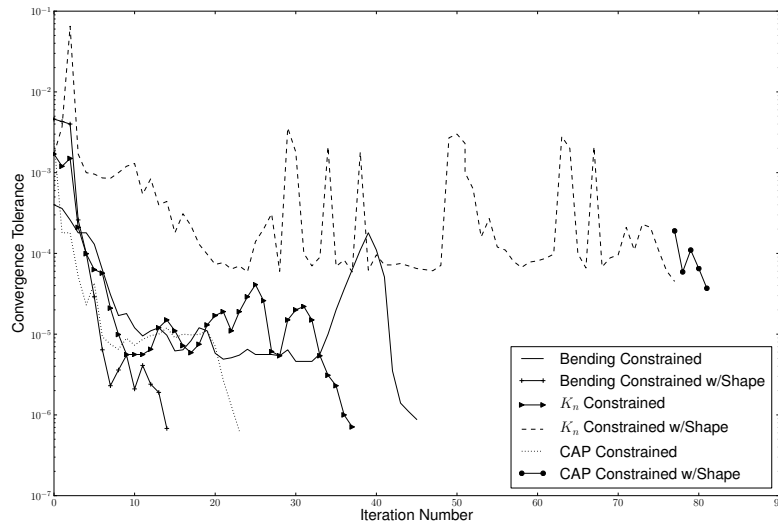**Table 10. NACA 0012 wing: Shape optimization results, 1107 k cells, M = 0.85**

Figure 23. Optimization convergence history: M = 0.7

References

[1] Liebeck, R. H., "Design of the Blended Wing Body Subsonic Transport," *Journal of Aircraft*, Vol. 41, 2004, pp. 10–25.

[2] Wakayama, S. and Kroo, I., "Subsonic Wing Planform Design Using Multidisciplinary Optimization," *Journal of Aircraft*, Vol. 32, No. 4, 1995, pp. 746–753.

[3] Wakayama, S. and Kroo, I., "The Challenge and Promise of Blended-Wing-Body Optimization," *AIAA Paper* 1998-4736, 1998.

[4] Perez, R. E., Liu, H. H., and Behdinan, K., "Multidisciplinary Optimization Framework for Control-Configuration Integration in Aircraft Conceptual Design," *Journal of Aircraft*, Vol. 43, No. 6, 2006, pp. 1937–1948.

[5] Jameson, A., "Aerodynamic Design via Control Theory," *Journal of Scientific Computing*, Vol. 3, No. 3, 1988, pp. 233–260.

[6] Reuther, J. J., Jameson, A., Alonso, J. J., Rimlinger, M. J., and Saunders, D., "Constrained Multipoint Aerodynamic Shape Optimization Using an Adjoint Formulation and Parallel Computers, Part 1," *Journal of Aircraft*, Vol. 36, No. 1, 1999, pp. 51–60.

[7] Reuther, J. J., Jameson, A., Alonso, J. J., Rimlinger, M. J., and Saunders, D., "Constrained Multipoint Aerodynamic Shape Optimization Using an Adjoint Formulation and Parallel Computers, Part 2," *Journal of Aircraft*, Vol. 36, No. 1, 1999, pp. 61–74.

[8] Hicken, J. E. and Zingg, D. W., "Induced-Drag Minimization of Nonplanar Geometries Based on the Euler Equations," *AIAA Journal*, Vol. 48, No. 11, 2010, pp. 2564–2575. doi:10.2514/1.J050379.

[9] Martins, J. R. R. A., Alonso, J. J., and Reuther, J. J., "High-Fidelity Aerostructural Design Optimization of a Supersonic Business Jet," *Journal of Aircraft*, Vol. 41, No. 3, 2004, pp. 523–530.

[10] Kenway, G. K. W., Kennedy, G. J., and Martins, J. R. R. A., "A Scalable Parallel Approach for High-Fidelity Aerostructural Analysis and Optimization," *53rd AIAA/ASME/ASCE/AHS/ASC Structures, Structural Dynamics, and Materials Conference*, Honolulu, HI, April 2012, AIAA 2012-1922.

[11] Liem, R. P., Kenway, G. K., and Martins, J. R. R. A., "Multi-point, multi-mission, high-fidelity aerostructural optimization of a long-range aircraft configuration," *Proceedings of the 14th AIAA/ISSMO Multidisciplinary Analysis and Optimization Conference*, Indianapolis, IN, Sept. 2012. doi:10.2514/6.2012-5706, AIAA 2012-5706.

[12] Mader, C. A. and Martins, J. R. R. A., "Stability-Constrained Aerodynamic Shape Optimization of a Flying Wing Configuration," *Proceedings of the 13th AIAA/ISSMO Multidisciplinary Analysis and Optimization Conference*, Fort Worth, TX, 2010, AIAA 2010-9199.

[13] Mader, C. A. and Martins, J. R. R. A., "Derivatives for Time-Spectral Computational Fluid Dynamics Using an Automatic Differentiation Adjoint," *AIAA Journal*, Vol. 50, December 2012, pp. 2809–2819. doi:10.2514/1.J051658.

[14] Perez, R. E., Jansen, P. W., and Martins, J. R. R. A., "pyOpt: A Python-Based Object-Oriented Framework for Nonlinear Constrained Optimization," *Structures and Multidisciplinary Optimization*, Vol. 45, No. 1, 2012, pp. 101–118. doi:10.1007/s00158-011-0666-3.

[15] Gill, P. E., Murray, W., and Saunders, M. A., "SNOPT: An SQP Algorithm for Large-Scale Constrained Optimization," *SIAM Review*, Vol. 47, No. 1, 2005, pp. 99–131.

[16] Perez, R. E. and Martins, J. R., "pyACDT: An Object-Oriented Framework for Aircraft Design Modelling and Multidisciplinary Optimization," *Proceedings of the 12th AIAA/ISSMO Multidisciplinary Analysis and Optimization Conference*, Victoria, BC, September 2008, AIAA 2008-5955.

[17] Kenway, G. K., Kennedy, G. J., and Martins, J. R. R. A., "A CAD-Free Approach to High-Fidelity Aerostructural Optimization," *Proceedings of the 13th AIAA/ISSMO Multidisciplinary Analysis and Optimization Conference*, Fort Worth, TX, 2010, AIAA 2010-9231.

[18] Chai, S., Crisafulli, P., and Mason, W. H., "Aircraft Center of Gravity Estimation in Conceptual/Preliminary Design," *Proceedings of the 1st AIAA Aircraft Engineering, Technology, and Operations Congress*, Los Angeles, CA, 1995, AIAA 95-3882.

[19] Murman, S. M., "Reduced-Frequency Approach for Calculating Dynamic Derivatives," *AIAA Journal*, Vol. 45, No. 6, 2007, pp. 1161–1168.

[20] Da Ronch, A., Ghoreyshi, M., Badcock, K., Görtz, S., Widhalm, M., Dwight, R., and Campobasso, M., "Linear Frequency Domain and Harmonic Balance Predictions of Dynamic Derivatives," *Proceedings of the* 28th *AIAA Applied Aerodynamics Conference*, Chicago, IL, 2010, AIAA 2010-4699.

[21] Etkin, B., *Dynamics of Atmospheric Flight*, Dover Publications, Mineola, New York, 2000.

[22] Agenbag, D. S., *Longitudinal Handing Characteristics of a Tailless Gull-Wing Aircraft*, Master's thesis, University of Pretoria, Pretoria, South Africa, July 2008.

[23] McRuer, D., Ashkenas, I., and Graham, D., *Aircraft Dynamics and Automatic Control*, Princeton University Press, Princeton, New Jersey, 1973.

[24] Bihrle, W., "A Handling Qualities Theory for Precise Flight Path Control," AFFDL Technical Report AFFDL-TR-65-198, 1966.

[25] United States Military, "Flying Qualities of Piloted Airplanes," Military Specification MIL-F-8785c, 1980.

[26] Martins, J. R. R. A. and Lambe, A. B., "Multidisciplinary design optimization: A Survey of architectures," *AIAA Journal*, 2013, (In press).

[27] Cramer, E. J., Dennis, J. E., Frank, P. D., Lewis, R. M., and Shubin, G. R., "Problem Formulation for Multidisciplinary Optimization," *SIAM Journal on Optimization*, Vol. 4, No. 4, 1994, pp. 754–776. doi:10.1137/0804044.

[28] Haftka, R. T., "Simultaneous Analysis and Design," *AIAA Journal*, Vol. 23, No. 7, 1985, pp. 1099–1103. doi:10.2514/3.9043.

[29] Braun, R. D. and Kroo, I. M., "Development and Application of the Collaborative Optimization Architecture in a Multidisciplinary Design Environment," *Multidisciplinary Design Optimization: State-of-the-Art*, edited by N. Alexandrov and M. Y. Hussaini, SIAM, 1997, pp. 98–116.

[30] Bloebaum, C. L., Hajela, P., and Sobieszczanski-Sobieski, J., "Non-Hierarchic System Decomposition in Structural Optimization," *Engineering Optimization*, Vol. 19, No. 3, 1992, pp. 171–186. doi:10.1080/03052159208941227.

[31] Sobieszczanski-Sobieski, J., Agte, J. S., and Sandusky, R. R., "Bi-Level Integrated System Synthesis," *AIAA Journal*, Vol. 38, No. 1, 2000, pp. 164–172. doi:10.2514/2.937.

[32] Kim, H. M., Michelena, N. F., Papalambros, P. Y., and Jian, T., "Target Cascading in Optimal System Design," *Journal of Mechanical Design*, Vol. 125, No. 3, 2003, pp. 474–480. doi:10.1115/1.1582501.

[33] Lambe, A. B. and Martins, J. R. R. A., "Extensions to the Design Structure Matrix for the Description of Multidisciplinary Design, Analysis, and Optimization Processes," *Structural and Multidisciplinary Optimization*, Vol. 46, 2012, pp. 273–284. doi:10.1007/s00158-012-0763-y.